

MHONGOOSE discovery of a gas-rich low surface brightness galaxy in the Dorado group

F. M. Maccagni^{1,2,*}, W. J. G. de Blok^{1,3,4}, P. E. Mancera Piña⁵, R. Ragusa⁶, E. Iodice⁶, M. Spavone⁶, S. McGaugh⁷, K. A. Oman^{8,9,10}, T. A. Oosterloo^{1,4}, B. S. Koribalski^{11,12}, M. Kim¹³, E. A. K. Adams^{1,4}, P. Amram¹⁴, A. Bosma¹⁴, F. Bigiel¹⁵, E. Brinks¹⁶, L. Chemin¹⁷, F. Combes^{18,19}, B. Gibson²⁰, J. Healy¹, B. W. Holwerda²¹, G. I. G. Józsa^{22,23}, P. Kamphuis²⁴, D. Kleiner^{1,2}, S. Kurapati³, A. Marasco²⁵, K. Spekkens^{26,27}, S. Veronese^{1,4}, F. Walter²⁸, N. Zabel³, and A. Zijlstra²⁹

(Affiliations can be found after the references)

Received 31 January 2024 / Accepted 23 May 2024

ABSTRACT

We present the discovery of a low-mass, gas-rich low surface brightness galaxy in the Dorado group, at a distance of 17.7 Mpc. Combining deep MeerKAT 21-cm observations from the MeerKAT HI Observations of Nearby Galactic Objects: Observing Southern Emitters (MHONGOOSE) survey with deep photometric images from the VST Early-type Galaxy Survey (VEGAS) we find a stellar and neutral atomic hydrogen (HI) gas mass of $M_{\star} = 2.23 \times 10^6 M_{\odot}$ and $M_{\text{HI}} = 1.68 \times 10^6 M_{\odot}$, respectively. This low surface brightness galaxy is the lowest-mass HI detection found in a group beyond the local Universe ($D \gtrsim 10$ Mpc). The dwarf galaxy has the typical overall properties of gas-rich low surface brightness galaxies in the Local group, but with some striking differences. Namely, the MHONGOOSE observations reveal a very low column density ($\sim 10^{18-19} \text{ cm}^{-2}$) HI disk with asymmetrical morphology possibly supported by rotation and higher velocity dispersion in the centre. There, deep optical photometry and UV observations suggest a recent enhancement of the star formation. Found at galactocentric distances where in the Local Group dwarf galaxies are depleted of cold gas (at a projected distance of 390 kpc from the group centre), this galaxy is likely on its first orbit within the Dorado group. We discuss the possible environmental effects that may have caused the formation of the HI disk and the enhancement of star formation (SF), highlighting the short-lived phase (a few hundreds million years) of the gaseous disk, before either SF or hydrodynamical forces will deplete the gas of the galaxy.

Key words. galaxies: dwarf – galaxies: evolution – galaxies: formation – galaxies: kinematics and dynamics

1. Introduction

In the hierarchical model of galaxy evolution, dwarf galaxies ($M_{\star} \lesssim 10^9 M_{\odot}$) are the most abundant in the Universe and form the building blocks of more massive galaxies, such as our own Milky Way (MW). Dwarf galaxies typically have dynamical masses more than four times larger than their baryonic mass (e.g. Das et al. 2020), which makes them ideal laboratories in which to test cosmological evolution and model dark matter (DM), which accounts for up to $\sim 27\%$ of the total energy density of the Universe (e.g. Planck Collaboration VI 2020). Nevertheless, little is known about the formation and evolution of these low-mass galactic systems. Dwarf galaxies can be strongly and rapidly affected by their environments. Tidal interactions, for example, are known to generate a specific class of dwarf galaxies (i.e. tidal dwarfs) that in their formation are depleted of DM (e.g. Duc & Mirabel 1998; Read et al. 2017; Venhola et al. 2017; Buck et al. 2019; Gray et al. 2023). Conversely, hydro-dynamical interactions with the intergalactic medium (IGM) can strip and deplete the gaseous disks of these galaxies (e.g. McConnachie et al. 2007; Westmeier et al. 2011; Józsa et al. 2021; Yang et al. 2022). Dwarfs, then, help us build a complete picture of how the environment affects the availability of their gas reservoir, ultimately regulating their star formation history. They are fundamental to understanding the dynamical processes driving the assembly of the stellar and gaseous disks of galaxies.

The new generation of wide-field optical imaging surveys, such as the Dark Energy Survey (DES, e.g. Dey et al. 2019; Martínez-Delgado et al. 2023) or the VST Early-type Galaxy Survey (VEGAS, e.g. Capaccioli et al. 2015; Iodice et al. 2020) have enabled the discovery and study of the stellar component of hundreds of dwarf galaxies down to very low surface brightnesses, that is $\sim 27\text{--}29 \text{ mag/arcsec}^2$ in the g-band (Forbes et al. 2020; Iodice et al. 2021). However, the analysis of the gaseous component, which is the best tracer for the kinematics and consequently the DM halo and environment, has been much more difficult. A galaxy at the low-mass end of the population ($M_{\star} \lesssim 10^7 M_{\odot}$), with a gas fraction of 50%, would require a sensitivity to neutral atomic gas masses of $M_{\text{gas}} \lesssim 5 \times 10^6 M_{\odot}$. Hence, a search for the HI in these sources has been limited so far only to the nearby Universe ($\lesssim 10$ Mpc) and by the sensitivities of HI surveys such as, for example, the Westerbork observations of Neutral Hydrogen in Irregular and SPiral galaxies (WHISP, Swaters et al. 2002), the Very Large Array survey of Advanced Camera for Surveys Nearby Galaxy Survey Treasury galaxies (VLA-ANGST, Ott et al. 2012), the ‘(almost) dark galaxies in the ALFALFA survey’ (Leisman et al. 2017), The Local Volume HI Survey (LVHIS; Koribalski et al. 2018), Apertif (Adams et al. 2022), and the Wide-field ASKAP L-band Legacy All-sky Blind Survey (WALLABY; Westmeier et al. 2022). Only in a handful of dwarf galaxies have resolved studies of the bulk of their HI kinematics been possible, such as, for example, in the sample of The HI Nearby Galaxy Survey of the Local Irregulars That Trace

* Corresponding author; filippo.maccagni@inaf.it

Luminosity Extremes (LITTLE THINGS; Hunter et al. 2012; Oh et al. 2015; Iorio et al. 2017), the dwarf galaxies of LVHIS and VLA-ANGST (Mancera Piña et al. 2021), or in, for example, Leo T (Ryan-Weber et al. 2008; Adams & Oosterloo 2018) and Leo-P (Bernstein-Cooper et al. 2014).

Recently, the combination of deep 21-cm HI observations ($N_{\text{HI}} \lesssim 10^{19} \text{ cm}^{-2}$) with deep optical photometry ($\mu_r \gtrsim 27 \text{ mag/arcsec}^2$) allowed us to discover several new gas-rich and low-mass low-surface-brightness objects beyond the Local Group (LG). The MeerKAT Fornax Survey (Serra et al. 2023), for example, has investigated the HI counterparts of all dwarf galaxies in the Fornax cluster ($D \sim 20 \text{ Mpc}$) down to an HI mass limit of $M_{\text{HI}} \sim 5 \times 10^5 M_{\odot}$ (Kleiner et al. 2023), which were discovered and catalogued by the optical Fornax Deep Survey down to a surface brightness limit of $\sim 26 \text{ mag/arcsec}^2$ in the r -band (Venhola et al. 2017, 2022).

In clusters, the environment strongly affects the HI content of dwarf galaxies. In Virgo, for example, the HI disks of dwarfs are stripped by ram pressure (RP) by the IGM even in the low-density outskirts of the cluster (Boselli et al. 2008a,b). In the less dense medium of Fornax, tidal and hydrodynamical interactions efficiently deplete the HI in dwarf galaxies in between a few tens of millions of years and a few hundred million years (Kleiner et al. 2023). The study of low-mass objects in groups and in the field is so far more incomplete, the main limitation being the difficulty in reaching very deep optical and HI surface brightness limits and in covering, at the same time, a wide-enough field of view to be able to discover these sources, which are often found hundreds of kilo-parsecs away from their host galaxies. The MeerKAT HI Observations of Nearby Galactic Objects: Observing Southern Emitters survey (MHONGOOSE, de Blok et al. 2016, 2020, 2024) is now providing us with the unique opportunity to discover low HI mass sources ($M_{\text{HI}} \sim 10^6 M_{\odot}$) within $1 \times 1 \text{ deg}^2$ of 30 nearby star forming galaxies (median distance $D = 10.3 \text{ Mpc}$). Because of the sensitivity to diffuse HI emission over the full field of view guaranteed by MeerKAT, MHONGOOSE investigates the gaseous environment of these galaxies out to almost their virial radius. The coincidence of the HI gas detected in the environment with the optical counterpart detected by sensitive optical observations ($\mu_r \gtrsim 27 \text{ mag/arcsec}^2$) allows us to construct a complete census of the low-mass gas-rich galaxy population around the target galaxies. The MHONGOOSE galaxies are mostly isolated or live in nearby sparse groups and span an HI mass range between 10^6 and $10^{11} M_{\odot}$. The first data release of the shallow observations of the first 10% of the MHONGOOSE data already mapped tens of companion satellite galaxies (de Blok et al. 2024).

In this paper, we present the discovery of the lowest HI mass system ($M_{\text{HI}} = 1.68 \times 10^6 M_{\odot}$) with an optical counterpart detected in the Dorado group ($D = 17.69 \text{ Mpc}$, e.g. Rampazzo et al. 2020) by the MHONGOOSE deep observations of the star-forming spiral galaxy NGC 1566. This group was observed in the neutral hydrogen by previous surveys (e.g. Kilborn et al. 2005; Elagali et al. 2019), but never with the depth and resolution provided by MHONGOOSE, which led to the discovery of this and other HI counterparts of low-mass galaxies in the group. The newly discovered HI source (MKT 042326-551621) is the cold gas counterpart of the low surface brightness galaxy (LSBG) catalogued, for example, in Tanoglidis et al. (2021) with source number 19696. The authors associated this source with the density peak of their distribution of LSBGs in the surroundings of the Fornax cluster, at 19 Mpc. For the very first time, because of the HI systemic velocity of this source, we can determine that LSB-D lies in the outskirts of the Dorado group.

Given its location in Dorado, and its low-surface-brightness nature, we name this galaxy LSBG-Dorado-A, and for brevity, we hereafter refer to it as LSB-D.

Deep optical observations from VEGAS of the Dorado group allow us to study the optical counterpart of the HI detection. This galaxy is the least-massive low surface brightness galaxy ($M_{\star} \sim 2.45 \times 10^6 M_{\odot}$) with highest gas fraction ($f_{\text{gas}} = M_{\text{gas}}/(M_{\text{gas}} + M_{\star}) = 0.48$) detected beyond the Local Group. Thanks to the high sensitivity and resolution of both MeerKAT and VST observations we are able to resolve and study in detail the HI gas of such a small object in Dorado and relate its morphology and kinematics to its star formation history and evolution within the group's environment.

This paper is structured as follows: in Sect. 2, we present the MeerKAT HI and optical VST observations and show the morphology and kinematics of the HI in LSB-D and its optical and star formation properties. In Sect. 3 we discuss the location of this dwarf galaxy within the Dorado group, its baryon content and we present possible scenarios on the evolution of its HI disk and SF. Section 4 summarizes the results and examines the possible studies of low-mass sources that are being opened by these novel deep HI and optical observations.

2. Observations and results

2.1. MHONGOOSE neutral hydrogen observations

The 21-cm MeerKAT (Camilo et al. 2018; Mauch et al. 2020) observations presented in this paper were taken as part of the MHONGOOSE survey targeting the massive lopsided spiral galaxy NGC 1566 ($M_{\text{HI}} = 1.1 \times 10^{10} M_{\odot}$, $D_{\text{NGC1566}} = 17.6 \text{ Mpc}$ Elagali et al. 2019; Anand et al. 2021). NGC 1566 was observed for 55 hours in ten separate 5.5 hour tracks reaching HI column density sensitivities of $N_{\text{HI}}(3\sigma) \sim 6 \times 10^{18} \text{ cm}^{-2}$ at $30''$ resolution, over 16 km s^{-1} .

A complete description of the data reduction of the MHONGOOSE observations is given in the survey paper (de Blok et al. 2024). Here, we summarise the main steps taken to produce the HI datacubes¹ that led to the detection of the gas rich low surface brightness galaxy LSB-D. We reduce the data using CARACal (Józsa et al. 2020), a containerised pipeline written in Python3. CARACal is set up in a modular fashion allowing us to use tasks from different radio astronomical packages for each step of the data reduction. The data-reduction steps are performed on a single node of the MeerGas cluster (128 cores, 1 Tb RAM). All ten tracks are reduced following the same strategy and using the same set of parameters, except for a few minor exceptions.

The data reduction procedure is divided in three parts. The first part is performed on the single 5.5 hours tracks and consists of cross-calibration, RFI-flagging, self-calibration and continuum subtraction. The second part consists of combining all ten observations together in the uv -space, followed by the joint deconvolution and imaging to produce HI datacubes at multiple resolutions with a 1.4 km s^{-1} channel width, without further continuum subtraction. In the third part, we create the moment maps (i.e. HI flux density, velocity field and HI line-width map) of the imaged field of view ($1.5 \times 1.5 \text{ deg}^2$) using the automated source finder SoFIA-2 (Westmeier et al. 2021).

We produce the final datacubes with six weighting and tapering combinations, that span resolutions from $90''$ to $7''$, with 3σ sensitivity limits ranging from $5 \times 10^{17} \text{ cm}^{-2}$ to $5 \times 10^{20} \text{ cm}^{-2}$ over

¹ The datacubes span approximately 720 channels (or a 1000 km s^{-1} velocity range) centred on the target galaxy.

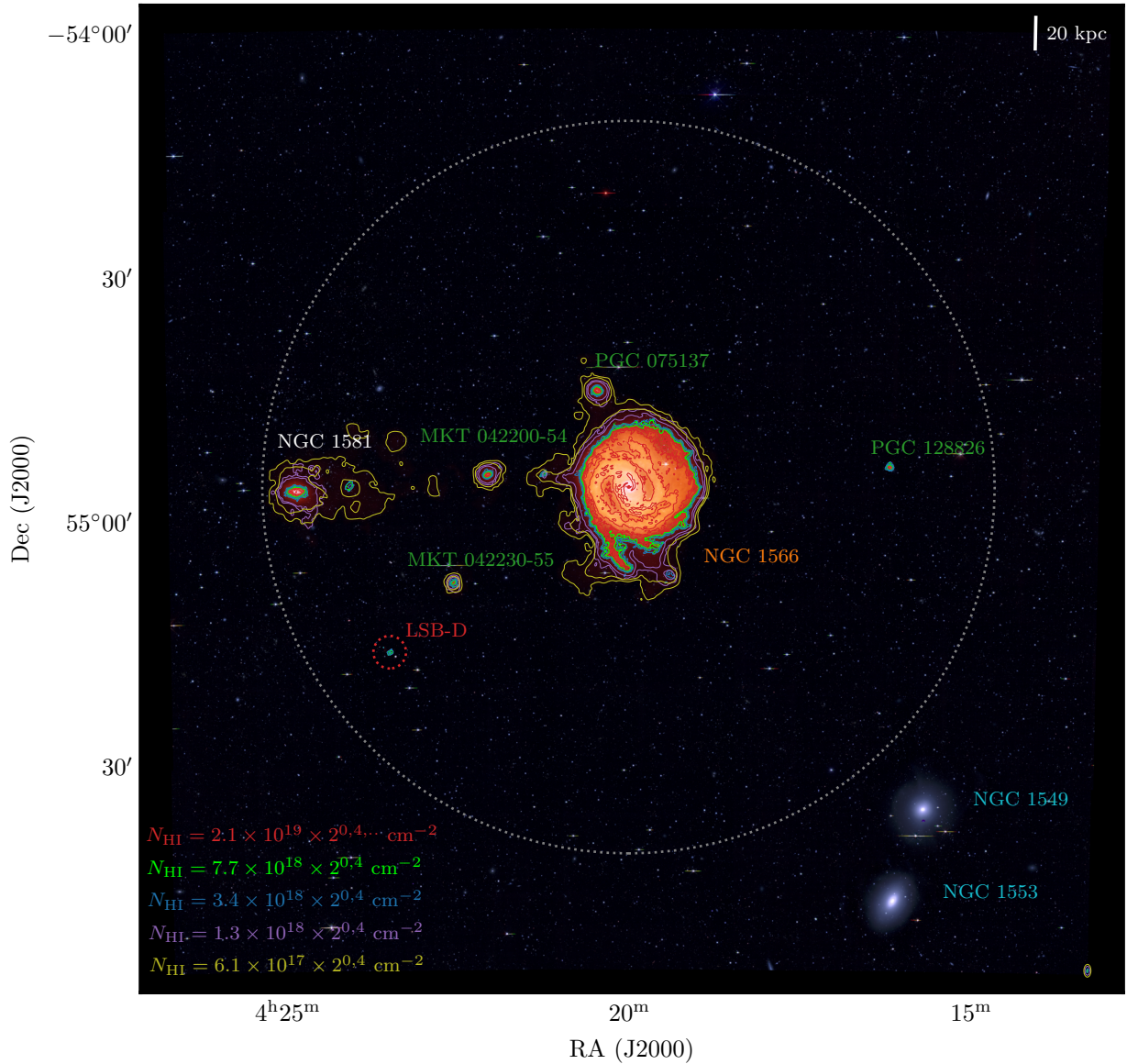


Fig. 1. Primary beam corrected flux-density HI emission detected by MeerKAT within a $1.5 \times 1.5 \text{ deg}^2$ field centred on NGC 1566 (the imaged f.o.v. is marked by the dashed grey circle), overlaid on the DECaLS optical image in the g, r, z filters. The HI emission is a composite of flux-density maps derived from the multi-resolution datacubes. The resolutions shown by coloured contours are $12'' \times 10''$ (red), $25'' \times 18''$ (green), $32'' \times 23''$ (blue), $65'' \times 64''$ (purple), $94'' \times 92''$ (yellow-green). For resolutions between $\sim 90''$ and $25''$ two contours are shown, i.e., $N_{\text{HI}} = 3\sigma \times 2^n$ with $n = 0, 2$. The $12'' \times 10''$ resolution has further increasing contours ($n = 0, 2, 4, \dots$). The PSF of the multi-resolution maps are shown in the bottom-right corner with the same colour coding. Details on the HI properties of the sources in the field are given in Table A.2.

16 km s^{-1} , respectively (further details are given in Appendix A). We use SoFiA-2 to search for HI detections with a smooth & clip algorithm, with Gaussian kernels 1, 2 and 3 times the spatial resolution of the cubes. The detection threshold is set to 3.5 times the noise (evaluated in 3D over a spectral window of 7 channels). All HI sources detected in the field of view have a detection reliability of 85%, based on the distribution of positive and negative noise peaks in the datacubes (see Serra et al. 2015; Westmeier et al. 2021, for details on the reliability estimate). We verify that SoFiA-2 identified all genuine HI emission by also visually inspecting the datacubes in virtual reality (Jarrett et al. 2021, iDaVIE).

The HI flux density distribution of NGC 1566 and of the galaxies detected by MeerKAT at resolutions between $90''$ to $7''$ is shown in Fig. 1 over a combination of the g, r, z opti-

cal observations of the Dorado group from the Dark Energy Camera Legacy Survey (dr10-DECaLS). The doublet of early-type galaxies NGC 1549 and NGC 1553 in the centre of the group is shown in the south-west, beyond the imaged MeerKAT field of view (dashed circle). New HI detections are marked in green. The first contour of each colour (from yellow-green to red) shows the $S/N = 3$ HI column density limit of datacubes at resolutions between $90''$ and $12''$. MeerKAT has a primary beam diameter of 1 degree (at this diameter the sensitivity of the array drops to 50%). This enables us to study not only NGC 1566 and its interactions with its nearby satellites, but also to investigate in detail its environment out to ~ 360 projected-kpc, which corresponds approximately to 75% of its radius at 500 times the critical density of the Universe at the current epoch ($r_{500} = 0.47 \text{ Mpc}$, Kilborn et al. 2005).

Table 1. Properties of the Dorado group.

Parameter	Value
Centre RA [J2000]	04 ^h 16 ^m 10 ^s
Centre Dec [J2000]	−55 ^d 46 ^m 48 ^s
Group Members	31
Morphological classification ^(†)	16 ETG/10 LTG/5 Uncl.
$\langle v_{\text{hel}} \rangle$ [km s ^{−1}]	1231
D [Mpc]	17.69
r_{vir} [kpc]	654
M_{vir} [M _⊙]	3.50×10^{13}
σ_{group} [km s ^{−1}]	282

Notes. The listed properties are taken from Kourkchi & Tully (2017), where formulae and definitions to the parameters are provided. The centre of Dorado coincides with S0 galaxy NGC 1553, which has as close-by companion the BGG NGC 1549. The reported group distance and heliocentric velocity are based on the unweighted averaging of the radial velocities of their members. ^(†)Morphological classification of group members divided in early-type galaxies (ETG), late-type galaxies (LTG) and unclassified (Uncl.) (Rampazzo et al. 2020).

The HI MHONGOOSE observations of NGC 1566 are the deepest and highest resolution 21-cm observations available so far of this galaxy (a summary of the sensitivities is shown in Table A.1). They improve our characterization of the low-column densities features of its HI disk of at least an order of magnitude (Elagali et al. 2019) and allow us to detect HI associated with several satellites, as well as diffuse HI tails tracing past interactions (as in NGC 1581, in the east of the field of view, Fig. 1). A full description of the cold gas distribution and kinematics of NGC 1566 and the other detections will be given in a following paper, a summary of their HI properties is shown in Table A.2.

Among the new sources, to the south-east of NGC 1566, at 186 kpc in projection at coordinates RA = 04^h23^m26^s, Dec = −55^d16^m21^s, lies the lowest HI detection associated with a galaxy made by MHONGOOSE so far, the aforementioned LSB-D (circled in red in Fig. 1). Deep optical observations allow us to identify that the HI gas is co-located with a low surface brightness galaxy. The HI systemic velocity of LSB-D ($v_{\text{sys}} = 1214 \text{ km s}^{-1}$) is consistent with the average recession velocity of the Dorado group ($v_{\text{hel}} = 1269 \text{ km s}^{-1}$) and the source seems to be located at its outskirts. Dorado is a loose group with centre coincident with the S0 galaxy NGC 1553 (visible in the south-west in Fig. 1), which forms a pair with the brightest group galaxy (BGG) NGC 1549 (Firth et al. 2006; Kourkchi & Tully 2017). LSB-D is located to the north-east of Dorado’s centre (68′ away, see Fig. 1), whereas NGC 1566 and its companions are at a distance of 35′. A summary of the main properties of Dorado is shown in Table 1.

The HI disk of LSB-D is detected at resolutions between 10 and 40 arcseconds with peak signal-to-noise $S_{\text{peak}}/N \gtrsim 5$, while the gas becomes too beam-diluted to be detected at the lowest resolutions and below the detection limit at the highest resolution of our datacubes (7′). This highlights the compact but diffuse nature of the HI disk, see Sect. 3.2 for further details. In what follows, we analyse the results only from the 25′ × 18′ resolution datacube, with 1.4 km s^{−1} channel-width generated with no tapering and a robustness parameter of 1.0, (Briggs et al. 1999, see Table A.1). At this resolution, we fully recover the total extent of the HI, spatially resolving it with 3 beam elements, while at higher resolutions we resolve out part of the disk. The

noise in the primary beam corrected cube close to LSB-D is 0.265 mJy beam^{−1}. In Appendix B we show the channel maps of the HI emission of LSB-D.

2.2. HI properties of LSB-D

The integrated HI spectrum of LSB-D is shown in Fig. 2. The HI line spans over 17 channels (1.4 km s^{−1} wide) with a full-width at zero intensity (FWZI) of $w_{\text{FWZI}} = 24 \text{ km s}^{-1}$. The profile is double-peaked suggesting the gas may be rotating within the galaxy and an extended tail is present at blueshifted velocities. The total flux density of the HI line is $S_{1.4\text{GHz}}\Delta\nu = 22.9 \text{ mJy km s}^{-1}$. The HI properties of LSB-D are summarized in Table 2.

In a group, the projected line of sight velocity we measure from the HI line is the composition of the systemic velocity of the source and its relative projected motion within the group. The exact trajectory of LSB-D is unknown, but since its systemic velocity ($v_{\text{sys, LSB-D}} = 1214 \text{ km s}^{-1}$) is similar to that of the group centre ($v_{\text{sys, NGC1553}} = 1201 \text{ km s}^{-1}$), and of the close-by BGG NGC 1549 ($v_{\text{sys, NGC1549}} = 1202 \text{ km s}^{-1}$), it is reasonable to approximate its distance by that of the group centre ($D = 17.69 \text{ Mpc}$)², which has been estimated by averaging the radial velocities of their group members (Kourkchi & Tully 2017; Rampazzo et al. 2020). At this distance LSB-D lies in projection 351 kpc away from NGC 1553 and 181 kpc and 116 kpc from NGC 1566 and NGC 1581, respectively ($v_{\text{sys, NGC1566}} = 1496 \text{ km s}^{-1}$, $v_{\text{sys, NGC1581}} = 1609 \text{ km s}^{-1}$). Further information on the location of LSB-D within the group is given in Sect. 3.1.

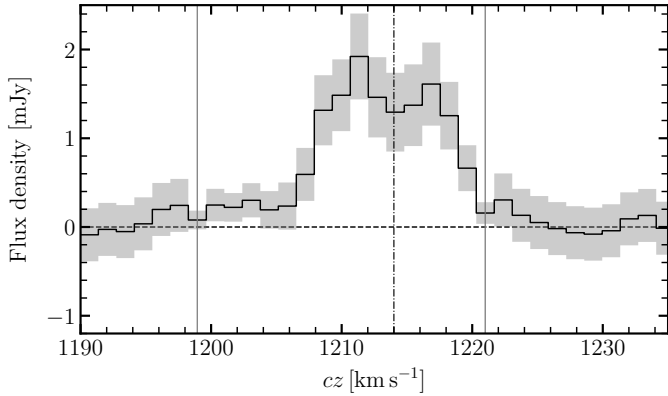
Following standard equations (e.g. Meyer et al. 2017), the total flux of LSB-D corresponds to an HI mass of $M_{\text{HI}} = 1.68 \times 10^6 M_{\odot}$. So far, this is the lowest HI mass that has been associated with a low surface brightness galaxy beyond the Local Group. For comparison, the typical dwarf population in the LG has associated HI masses two orders of magnitudes higher than in LSB-D, with only a few sources with $M_{\text{HI}} \sim 10^6 M_{\odot}$ (e.g., Bouchard et al. 2006; Grevech & Putman 2009; Hunter et al. 2012; Spekkens et al. 2014; Iorio et al. 2017).

The left panel of Fig. 3 shows the HI and optical body of LSB-D in detail. The first contour shows the $S/N = 3$ flux-limit (before primary beam correction) at 25′ × 18′, which corresponds to a column density of $N_{\text{HI}} = 4.6 \times 10^{18} \text{ cm}^{-2}$. Further details on the spatial and velocity extent of LSB-D are visible in the channel maps (Fig. B.2). The HI gas is distributed in an irregular morphology that at first look resembles a disk with projected major axis $a = 36''$ ($D_{\text{HI}} = 2.8 \pm 0.8 \text{ kpc}$), and minor axis $b = 22'' = 1.8 \pm 0.8 \text{ kpc}$. The major axis is misaligned with respect to the optical body ($PA_{\text{HI}} = 141^\circ$ and $PA_{\star} = 190^\circ$). Along the minor axis, in the north-east, the HI elongates in a low-column density cloud ($N_{\text{HI}} = 3\text{--}9 \times 10^{18} \text{ cm}^{-2}$). This cloud contributes to the blue-shifted tail in the HI spectral profile (Fig. 2), and is visible in the channel maps at velocities 1209 km s^{−1} and 1212 km s^{−1}. We highlight that also a low-mass HI cloud without associated stars may be present (at the detection limit of our observations) 8′ further north of LSB-D (41-projected kpc) at coordinates RA = 04^h22^m31^s, Dec = −55^d12^m02^s. The integrated spectrum is shown in Fig. B.1 and has full-width at zero intensity of 18 km s^{−1}. The total estimated HI mass is $3.65 \times 10^5 M_{\odot}$, which is slightly higher than the 3 σ detection limit over 16 km s^{−1} of the observations.

² At this distance, the image scale is 85 parsec/arcsec assuming a Λ CDM cosmology, with Hubble constant $H_0 = 70 \text{ km s}^{-1} \text{ Mpc}^{-1}$ and $\Omega_{\Lambda} = 0.7$ and $\Omega_{\text{M}} = 0.3$.

Table 2. HI properties of LSB-D.

Parameter	Value
Right Ascension [J2000]	04 ^h 23 ^m 26 ^s
Declination [J2000]	−55 ^d 16 ^m 29 ^s
D [Mpc]	17.69
HI systemic velocity [radio, km s ^{−1}]	1214
Total flux density [mJy km s ^{−1}]	22.9 ± 10%
M_{HI} [M _⊙]	1.68 × 10 ⁶
M_{bar} [M _⊙]	4.68 × 10 ⁶
v_{rot} [km s ^{−1}]	9.0 ± 3.5
$\sigma_{\text{HI}}^{(\dagger)}$ [km s ^{−1}]	3 ± 1.4
PA (HI disk position angle, °)	141 ± 5
i (HI disk inclination, °)	50 ± 15
$a/2$ (HI semi-major axis) [kpc]	1.4 ± 0.8
$b/2$ (HI semi-minor axis) [kpc]	0.94 ± 0.8
f_{gas} (gas fraction)	0.48

Notes. ^(†): average value across the HI disk, in the centre $\sigma = 5.5 \pm 1$ km s^{−1}.

Fig. 2. Integrated spectrum of LSB-D, with its noise per channel (grey shaded region). The vertical dashed line shows the systemic velocity of the source ($v_{\text{sys}}^{\text{radio}} = 1214$ km s^{−1}), while the grey vertical lines show its full velocity range ($w_{\text{FWZI}} = 24$ km s^{−1}).

The right panel of Fig. 3 shows the velocity field of LSB-D. The HI gas is characterised by a gradient of velocities along the major axis. One interpretation is that regular rotating motions are ongoing in the gas. Nevertheless, some asymmetries are present in the velocity field with a deep V-shape penetrating the minor axis in the south-west. Independent of this, the morphology of the HI shown in the left panel of Fig. 3 is suggestive of a disk-like distribution. Under this assumption we assume we can then infer an inclination from the axis ratio (b/a), following, for example Sakai et al. (2000):

$$i = \cos^{-1} \sqrt{\frac{(b/a)^2 - q_0^2}{1 - q_0^2}} \quad (1)$$

where $q_0 = 0.13\text{--}0.27$ is the intrinsic minor-to-major axis ratio of edge-on spirals. Given the irregularity of the HI morphology, we determine the range of possible inclinations assuming the extreme values of the q_0 range and propagating the errors on the axis, which we estimate to be half the size of the beam minor axis, $9''$ (0.8 kpc). We obtain an inclination of $i = 50^\circ \pm 15^\circ$.

To further investigate the kinematics of the HI in LSB-D, we draw the position-velocity (PV) diagram across the major

($PA = 141^\circ$) and minor axis ($PA = 51^\circ$) of the HI disk (marked in the velocity field of Fig. 3 with a dashed and dashed-dotted line, respectively). The PV-diagram across the major axis (Fig. 4, top panel) shows a steep gradient of velocities which disappears in the PV-diagram along the minor axis (bottom panel of the Figure), this may indicate that the HI is supported by rotation. Along the velocity gradient, the HI is detected only over three consecutive channels (of 1.4 km s^{−1} each) indicating that the velocity dispersion is low ($\sigma = w_{50}/(2\sqrt{\ln 2}) \lesssim 3 \pm 1.4$ km s^{−1}) as typically found for the cold HI in rotating disks ($T < 1000$ K; Young et al. 2003; Warren et al. 2012). Under the assumption that rotation is (mostly) supporting the disk, a proxy for its rotational velocity can be inferred from the inclination-corrected velocity width (Sakai et al. 2000; Begum et al. 2008): $v_{\text{rot}} = 1/2 w_{20} \sin(i)^{-1} (1+z)^{-1}$ km s^{−1}. From the smooth gradient of velocities across the major axis we measure $w_{20} = 14$ km s^{−1} and $v_{\text{rot}} = 9.0 \pm 3.5$ km s^{−1}. Because of the difficulty in estimating the rotational velocity we estimate an error of $\sim 40\%$.

Figure 4 shows that in the centre, a second peak is present at $v = 1218$ km s^{−1} beyond the range of rotational velocities traced by the smooth gradient. Without considering the beam-smearing due to the turnover velocities in the central resolution beam, the second peak causes the velocity dispersion to increase to $\sigma = 5.5$ km s^{−1}. This central velocity dispersion is typical of low-mass systems (e.g. Iorio et al. 2017; Mancera Piña et al. 2021) and implies $v_{\text{rot}}/\sigma_v \sim 2$. This suggests that the central region of the HI disk has more turbulent kinematics, as also indicated by the shift of its centre with respect to the optical body (Fig. 3, left panel).

2.3. Deep optical data and stellar properties of LSB-D

Combining the deep HI observations with optical photometric observations we can state that LSB-D is without any reasonable doubt a gas rich low surface brightness galaxy. To properly characterize its stellar properties we rely on the deepest available photometric observations of the Dorado group from VEGAS (Spavone et al. 2017; Iodice et al. 2021). These observations reach sensitivities of the limiting surface brightness of $\mu_g = 28.9$ mag/arcsec², $\mu_r = 27.3$ mag/arcsec², in the g and r filters respectively, estimated for a point source at 5σ over a circular area with FWHM $\sim 1''$. These limits are approximately two magnitudes deeper than the DECaLS surface brightness limit (Martínez-Delgado et al. 2023). The VEGAS observations were acquired using the VST/OmegaCAM instrument (run ID: 0102.A-0669(A)), which has a total field of view (FoV) of $1^\circ \times 1^\circ$ and a spatial resolution of 0.214 arcsec/pixel (Kuijken 2011). The images were reduced using the dedicated *AstroWISE* pipeline (for details see McFarland et al. 2013; Venhola et al. 2017) specifically developed for the reduction of VST/OmegaCAM observations. The g and r bands were analysed by following the same procedure described in, for example, Ragusa et al. (2021, 2022, 2023), to which we refer for more details. In particular, the magnitudes are in the AB system, and are corrected for Galactic extinction using the coefficients from Schlafly & Finkbeiner (2011). The VEGAS g, r image of LSB-D is shown in Fig. 5.

We infer the optical properties of LSB-D with an isophote fitting procedure in the g and r bands. The surface brightness profiles are shown in the top panel of Fig. 6. The VEGAS observations confirm that the peak of the optical distribution of LSB-D is shifted with respect to the HI peak by ~ 0.4 kpc. We determine the stellar mass (M_*) from g and r magnitudes ($M_r = -13.47$, $M_g = -13.04$) following the procedure illustrated in

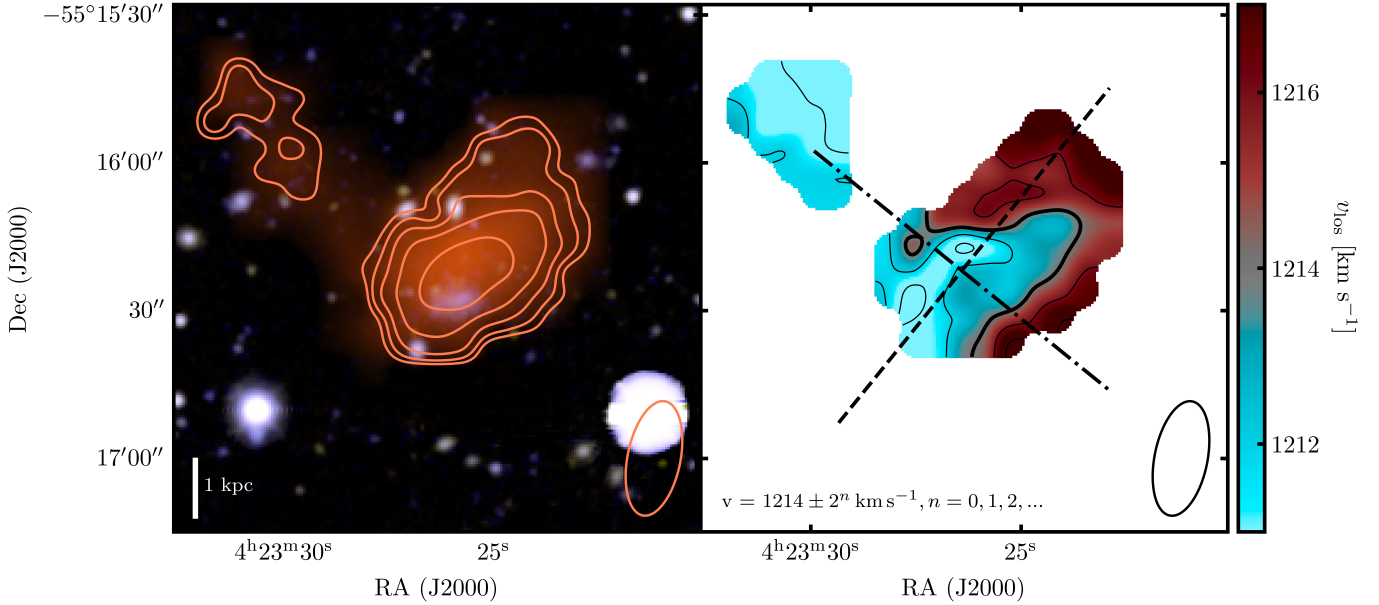


Fig. 3. *Left Panel:* DeCaLS optical image in the g, r, z filters overlaid with the HI contours from the $25'' \times 18''$ datacube used for the analysis in this paper. Levels increase as $4.6 \times 10^{18} \times 2^n \text{ cm}^{-2}$ ($n = 0, 1, 2, 3$), where the first contour marks the mean $S/N = 3$ detection limit. The PSF is shown in the bottom-right corner. Note the HI overlay in color with also the $32 \times 23''$ map. *Right Panel:* velocity field of the HI gas in LSB-D. The systemic velocity ($v_{\text{sys}} = 1214 \text{ km s}^{-1}$) is marked by the thick black iso-velocity contour, the other contour levels are shown in the bottom-left corner. The dashed and dashed-dotted lines mark the directions of the major (141°) and minor axes (51°) of the HI disk, respectively.

Into & Portinari (2013). Briefly, based on a mass-to-light (M/L) - color relationship, it is possible to derive an estimate of the average galaxy's M/L by using its $g-r$ color. This, in turn, leads to an estimate, passing through the luminosity, of a stellar mass $M_\star(r) = 2.2 \times 10^6 M_\odot$ and $M_\star(g) = 2.7 \times 10^6 M_\odot$, respectively. The stellar properties, along with the average $g-r$ colour, are listed in Table 3.

LSB-D has blue colours, similar to other nearby dwarf galaxies (e.g. Honey et al. 2018), and small effective radius, $r_{\text{eff}} = 0.5 \text{ kpc}$. Its radial colour profile (bottom panel of Fig. 6) shows a moderate reddening from the centre to the outskirts. Bluer colour in the centre suggest the presence of a younger stellar population or on-going star formation.

To further investigate this possibility, we examine if ultraviolet (UV) emission is associated with LSB-D in the *Galaxy Evolution Explorer Nearby Galaxy Survey* (Gil de Paz et al. 2007; Bianchi & Garcia 2014). Both in the far-UV ($\lambda \approx 154 \text{ nm}$, FUV) and near-UV ($\lambda \approx 231 \text{ nm}$, NUV) observations emission is detected in the HI disk of LSB-D, see the magenta and cyan contours in Fig. 5. Given its low-signal-to-noise, the UV observations on their own would unlikely have been considered a detection. Since the peak is present both in the FUV and in the NUV and is coincident with the centre and the stellar body of the galaxy, we consider the detection significant.

The higher velocity dispersion of the central HI gas may be due to the on-going or recent star formation suggested by the UV emission. The star formation rate (SFR) can be reliably estimated from the FUV emission (e.g. Leroy et al. 2019). We measure the UV-flux by centering a five-by-five pixel box on the peak, obtaining a total flux $F_{\text{FUV}} = 0.031 \text{ counts/sec}$. Correcting for extinction assuming a coefficient of $A_{\text{FUV}} = 0.13$ from Wall et al. (2019) and given that the GALEX observation has an average background emission (as measured in a few areas nearby the source) of $F_{\text{background}} = 0.00035 \text{ counts/sec}$, the corrected flux is $F_{\text{FUV}} = 0.025 \text{ counts/sec}$. We determine the SFR from the correlation with the FUV, as inferred from the cross-

matched sample of GALEX-SDSS galaxies (Salim et al. 2007; Leroy et al. 2008):

$$\text{SFR}_{\text{FUV}}^{\text{unobscured}} = 0.68 \times 10^{-28} L_\nu(\text{FUV}) M_\odot \text{ yr}^{-1} \quad (2)$$

where $L_\nu(\text{FUV})$ is in $\text{erg s}^{-1} \text{ Hz}^{-1}$. For LSB-D, $L_\nu(\text{FUV}) = 9.6 \times 10^{24} \text{ erg s}^{-1} \text{ Hz}^{-1}$, which gives $\log(\text{SFR})_{\text{LSB-D}} = -3.2 [M_\odot \text{ yr}^{-1}]$. LSB-D's SFR value is a factor of only a few below the SFR of the lowest mass MHONGOOSE target galaxies (see Table 1 of de Blok et al. 2024) and it is similar to the SFR in the low-mass end ($M_\star \lesssim 10^7 M_\odot$) of dwarf star-forming galaxies in the Local Universe (McQuinn et al. 2015a,b; Marasco et al. 2023).

3. Discussion

In this section we discuss the possible evolution of LSB-D and its HI disk as it can be inferred from its location within the Dorado group (Sect. 3.1), by its gaseous and stellar content (Sect. 3.2) and by its baryon-to-dark-matter content (Sect. 3.3). In Sect. 3.4, we present possible scenarios on the formation and evolution of its HI disk and on the enhancement of SF.

3.1. LSB-D in the Dorado group

LSB-D lies 390 projected-kpc to the north-east of the centre of Dorado (formed by the galaxy pair NGC 1549/NGC 1553), while the closest (in projection) massive galaxies NGC 1566 and NGC 1581 are 186 kpc and 190 kpc to the north-west and north-east, respectively. Since LSB-D is at the edge of their projected virial radii it has likely not yet tidally interacted with them. Figure 1 shows that LSB-D is too far away from other more massive group members to be considered their satellite. The closest galaxy to LSB-D is MKT 042200-545440 (also associated for the first time to Dorado thanks to our MeerKAT observations) which is a late-type galaxy with similar HI mass (see Table A.2).

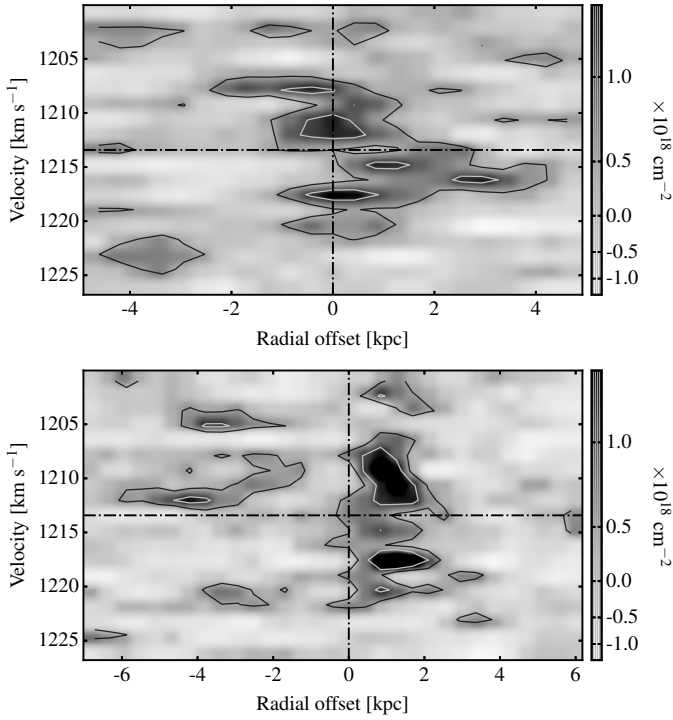


Fig. 4. *Top Panel:* position-velocity diagram taken along the major axis of the HI disk ($PA = 141^\circ$) with a slit of $20''$. Contour levels are at $5 \times 10^{17} \text{ cm}^{-2}$ and $1 \times 10^{18} \text{ cm}^{-2}$. *Bottom Panel:* position-velocity diagram taken along the minor axis of the HI disk ($PA = 51^\circ$) with an analogous slit, equal to the resolution of the observations. Contours are as in the top panel.

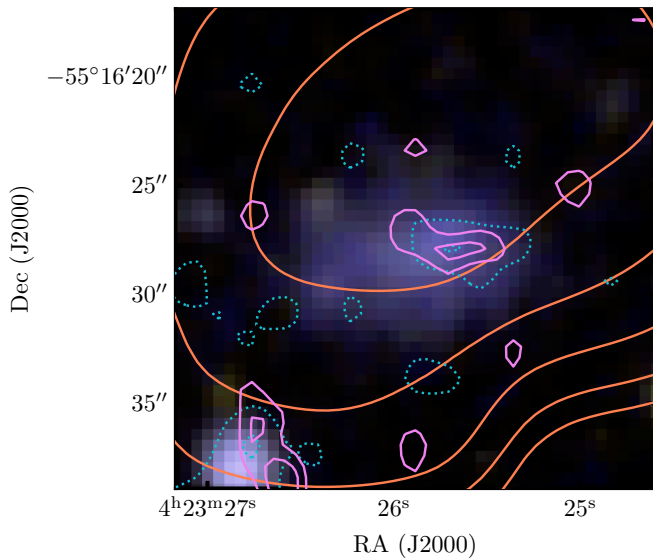


Fig. 5. VEGAS optical image in the g, r filters overlaid with the HI column density map. Orange contour levels are as the left panel of Fig. 3. In cyan and magenta contours we show the $S/N = 3$ and 5 contours from the NUV and FUV GALEX observations, respectively.

The phase-space diagram of Dorado can provide further insights related to the location of LSB-D and on its infall into the group. This diagram (see, for example, Jaffé et al. 2015) takes into account the distance and systemic velocity of the group members as well as the virial mass and velocity dispersion of Dorado ($M_{\text{vir}} = 3.5 \times 10^{10} M_{\odot}$, $R_{\text{vir}} = 528 \text{ kpc}$,

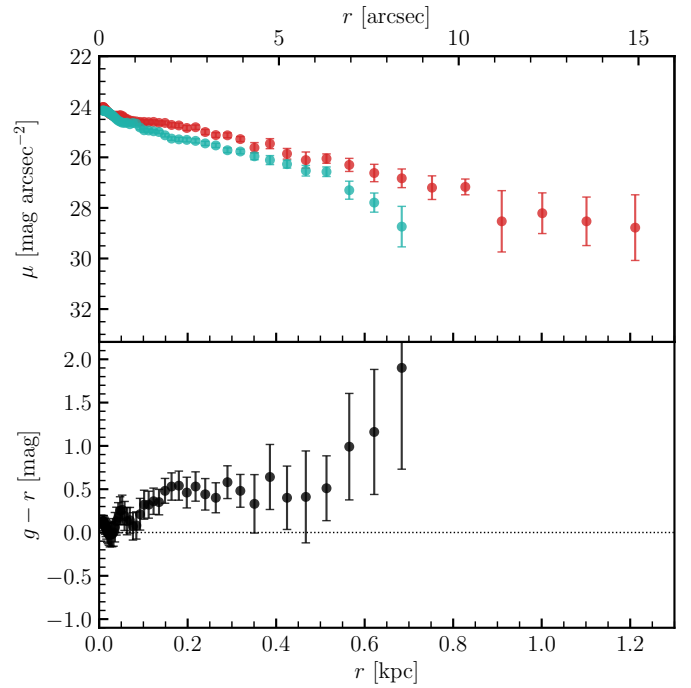


Fig. 6. *Top panel:* LSB-D's g and r radial surface brightness profile (cyan and red, respectively) inferred from the VEGAS observations. *Bottom panel:* radial $g - r$ colour profile measured out to $8''$ from the centre ($\sim 670 \text{ pc}$).

$\sigma_{\text{Dorado}} = 282 \text{ km s}^{-1}$) to understand where the sources are located in phase space with respect to the BGG, if they are already within its escape velocity, if they recently assembled into the group or if they have long been virialised. Figure 7 shows the phase-space diagram of all Dorado members as catalogued in Rampazzo et al. (2020, 2021, 2022) to which we add the sources newly associated with the group thanks to the MeerKAT observations, i.e. LSB-D, PGC 128826, PGC 075137, MKT 042200-545440, MKT 042230-550757, MKT 042326-551621. The Figure shows the caustic curves defined by the escape velocity of the group (which is derived from its virial mass and radius) and the virialized area of the group (dashed-dotted lines). As illustrated in Rhee et al. (2017), within this latter region it is more likely to find old members of the group between which interactions have already occurred, compared to recent infallers which are located between the virialized region and the caustic lines.

In the phase-space diagram, LSB-D is within the escape velocity of the group in the region of recent infallers. The recent infallers are expected to be more gas-rich than similar systems in the virialized region, since the environmental effects of the group (i.e. tidal interactions and/or ram pressure stripping) have not yet been strong enough or did not have enough time to deplete the sources of their gas.

To further investigate if LSB-D is a recent infaller of Dorado or if it had multiple orbits within the group, already, we estimate the probability distributions for orbital parameters and deprojected coordinates in group and clusters based on their phase space coordinates. In particular we follow the methodology illustrated in Oman et al. (2021, Sect. 3.2) (see also Oman et al. 2013). In brief, from an N -body simulation catalogue we select within an overdensity similar to Dorado all orbits of satellites with projected coordinates, host mass and satellite mass compatible with LSB-D. Further details on the selection

Table 3. Stellar properties of LSB-D.

Parameter	Value
M_r [mag]	-13.04 ± 0.25
M_g [mag]	-13.47 ± 0.11
$g - r$ [mag]	0.46 ± 0.21
$M_*(g)$ [M_\odot]	2.2×10^6
$M_*(r)$ [M_\odot]	2.7×10^6
$M/L(g)$ [M_\odot/L_\odot]	1.09
$M/L(r)$ [M_\odot/L_\odot]	1.09
r_{eff} [kpc]	0.5
μ_{eff} [mag''']	26
L_ν (FUV) [erg s $^{-1}$ Hz $^{-1}$]	9.6×10^{24}
$\log(\text{SFR}_{\text{FUV}})$ [$M_\odot \text{ yr}^{-1}$]	-3.2

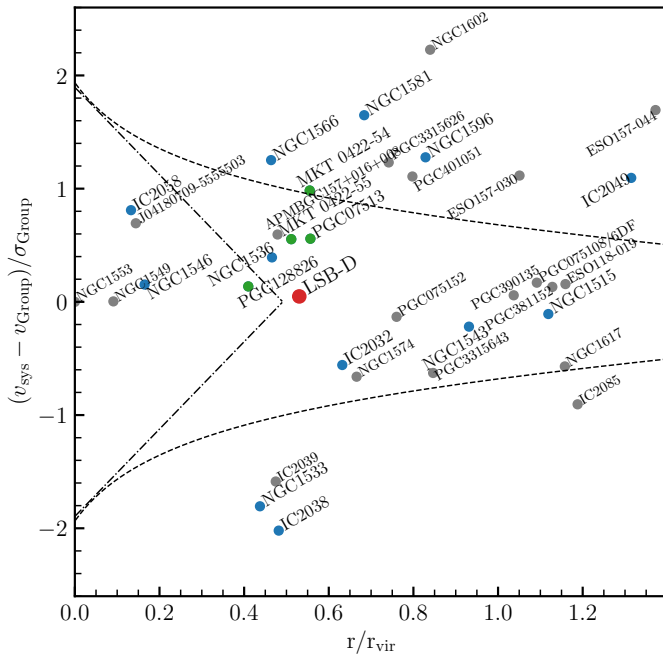


Fig. 7. Phase-space diagram of the Dorado group. LSB-D is shown in red, while previously known HI rich galaxies are shown in blue and new HI detections in green. The group's centre (NGC 1553) is at the zero coordinates, the dashed-dotted lines mark the virialised region of the Dorado group. The caustic curves (dashed lines) are defined by the escape velocity of the group.

constraints are given in Appendix C. From the distribution of deprojected coordinates of the selection, we derive the probability for the deprojected coordinates of LSB-D and for its orbit within the group. The median deprojected coordinates of LSB-D (with 16 – 84 percentile range) are $r_{3D} = 506_{-129}^{+481}$ kpc, $v_{3D} = 509_{-242}^{+208}$ km s $^{-1}$. These are shown in Fig. C.1 along with the distribution of the deprojected coordinates of all selected orbits. The probability for LSB-D to be an interloper ($r_{3D} > 2.5R_{\text{vir}}$) is $\leq 1\%$. The distribution of the pericentre of the selected orbits is bimodal with modes corresponding to either first or to second and later orbits. The probability for LSB-D to be past apocentre is $\sim 50\%$, but if it was within the first orbit the probability for LSB-D to be in the first infall before passing through the first pericentre is $\sim 27\%$, while the probability to be on the first orbit but past pericentre is $\sim 23\%$. In conclusion, the position in

the phase space diagram and the predictions on its deprojected coordinates suggest that LSB-D is a recent infaller of Dorado. The simulations suggest that in an overdensity similar to Dorado, galaxies with properties similar to LSB-D with those projected coordinates are typically found on their first or at the beginning of the second orbit within the group.

3.2. Gas and stellar content of LSB-D and its star formation rate

LSB-D belongs to the low-mass end of the HI-detected dwarf population. Here we compare its HI properties with its stellar content and with those dwarf galaxies in the Local Universe for which we have reliable estimates. In particular, we select sources from LITTLE THINGS (Oh et al. 2015; Iorio et al. 2017), SPARC (Spitzer Photometry and Accurate Rotation Curves, Lelli et al. 2016) and The HI Nearby Galaxy Survey (THINGS, Walter et al. 2008) samples, local low surface brightness galaxies (from McGaugh 2011; McGaugh et al. 2017) and ultra-diffuse galaxies (UDGs, from Mancera Piña et al. 2019, 2022b), for which we have precise estimates of the gas and stellar masses, as well as rotational velocities. The top panel of Fig. 8 shows the stellar mass against the gas mass for the mentioned samples and for LSB-D, which nicely fits on the one-to-one relation (shown by the dashed line). This Figure also highlights the low star and gas mass of LSB-D of which only a few analogues in the Local Universe have been studied in detail.

The baryonic Tully-Fisher (BTFR) relation links the baryonic mass of a galaxy with its rotational velocity (e.g. McGaugh et al. 2000; Ponomareva et al. 2018; Lelli et al. 2019). Whereas the relation is well established in the high mass regime (e.g. McGaugh 2012; McGaugh et al. 2021; Lelli 2022), its nature in the low-mass end is still a matter of heated debate as the scatter appears to increase towards lower masses (Geha et al. 2006; Begum et al. 2008; Mancera Piña et al. 2019). We investigate where LSB-D is located on the BTFR to understand if dynamically its overall properties are typical of the ones of the low-mass low surface brightness galaxies.

In the bottom panel of Fig. 8 we show the BTFRs from McGaugh et al. (2021):

$$v_0 = 0.379 \left(\frac{M_{\text{bar}}}{M_\odot} \right)^{1/4} \text{ km s}^{-1} \quad (3)$$

The double dashed line in the Figure takes into account that there is a factor of two offset between the velocity estimated from rotation or pressure supported systems (v_0 and σ , details are given in McGaugh et al. 2021). In Fig. 8 we added the samples from LITTLE-THINGS, THINGS, and SPARC keeping their selection parameters and estimates of the rotational velocity and baryonic masses (there is a negligible discrepancy with the BTFR estimated with different methods for the v_0 , Lelli et al. 2019). To this we also added the UDGs which are off the BTFR (Mancera Piña et al. 2019). LSB-D (shown in red) seems to be slightly offset with respect to the relation, even though because of the large uncertainties (in the inclination and rotational velocity of the HI disk) it can be consistent with the relation. We estimated LSB-D's baryonic mass and rotational velocity as follows. Since we do not spatially resolve the source with enough resolution elements to properly characterize its rotation curve (i.e. ~ 5 beams across the minor axis, see Bosma 1978; Sancisi et al. 2008), we estimate a rough dynamical mass enclosed in the LSB-D's HI disk as $M_{\text{dyn,rot}}(\leq r_{\text{HI}}) \sim \frac{r_{\text{HI}} v_{\text{rot}}^2}{G} \approx 2.6 \pm 1.0 \times 10^7 M_\odot$. Accounting for

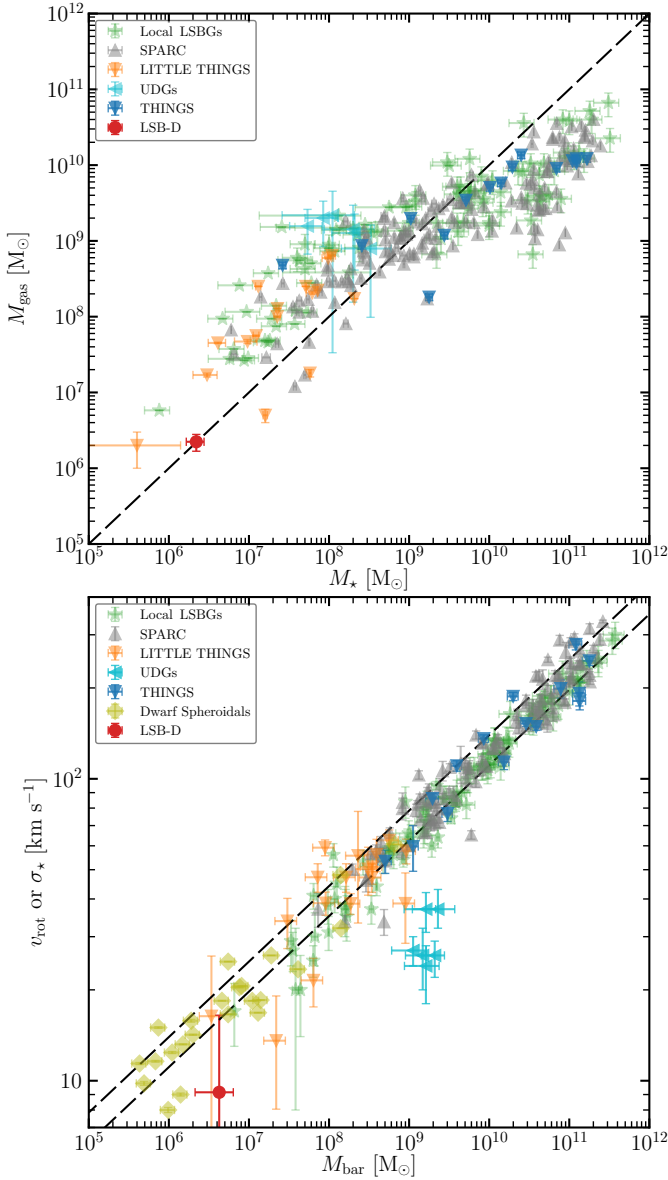


Fig. 8. *Top panel:* gas mass versus stellar mass for a sample of galaxies in the Local Universe. LITTLE-THINGS, SPARC and THINGS galaxies are marked by triangles (in orange, grey, and blue, respectively). Local low surface brightness galaxies (LSBGs) from [McGaugh \(2011\)](#), [McGaugh et al. \(2017, 2021\)](#) are in green, and UDGs in cyan. LSB-D is marked by the red circle. The dashed line marks the 1:1 linear relation. *Bottom panel:* the baryonic Tully-Fisher relation of Local Group dwarf and spiral galaxies (dashed line; [McGaugh et al. 2021](#)). Symbols are as in the top panel. For the Local LSBGs sample, pressure supported dwarfs (plotted against their velocity dispersion, σ_v) are marked by light green squares, while green triangles mark rotationally supported galaxies, plotted against their rotational velocity, v_{rot} .

helium ($M_{\text{gas}} = 1.33 \cdot M_{\text{HI}} = 2.23 \times 10^6 M_{\odot}$), the baryonic mass is $M_{\text{bar}} = M_{\text{gas}} + M_{\star} = 4.68 \times 10^6 M_{\odot}$ and the total gas fraction is $f_{\text{gas}} = M_{\text{gas}} / (M_{\text{gas}} + M_{\star}) = 0.48$. LSB-D is dark-matter dominated with its baryonic mass counting 5 – 10% of the dynamical mass. This is compatible, even though slightly higher, with other low surface brightness HI rich galaxies in the Local Universe ([Giovannelli et al. 2013](#); [Iorio et al. 2017](#)). Considering that LSB-D may not be fully supported by rotation (since in the centre $v_{\text{rot}}/\sigma_v \sim 2$), if we infer the dynamical mass from the maxi-

mum velocity dispersion through the virial theorem (as in other low-mass pressure supported systems, e.g. [McGaugh et al. 2021](#), also shown in the Figure), we obtain a similar result because of the low velocities of the gas along the disk.

The very low mass of LSB-D, the normality of its gaseous and stellar properties and compatibility with the baryonic Tully-Fisher relation shows the universality of the dynamical properties of galaxies which defines their evolution throughout the entire spectrum of masses, down to the smallest low surface brightness sources (albeit with larger scatter in this regime).

Overall, LSB-D shows normal gas, stellar and dynamical properties compared to Local Group galaxies. This suggests that LSB-D has undergone a ‘typical’ evolution throughout cosmic time, and that past recent interactions or the environment of Dorado have not influenced its halo or mass content significantly. Nevertheless, the optical and UV properties of LSB-D suggest, instead, that recently some event must have enhanced its star formation. Though gas rich by the standards of comparable low stellar mass galaxies (i.e. dwarf spheroidals in Fig. 8), LSB-D has slightly lower gas masses than the Local LSBGs of not too much greater stellar mass. However, the top panel of Fig. 9 shows that LSB-D is ≈ 0.8 dex above the M_{\star} -SFR relation defined by the Local LSBGs and THINGS galaxies. While it lies among the typically dwarf irregular LITTLE-THINGS galaxies³, some of the offset between LSB-D LITTLE-THINGS and the LSBGs and THINGS sample is due to the different tracers used to measure SF (FUV and $\text{H}\alpha$, respectively). For low-mass galaxies with $\log(\text{SFR}) \lesssim -2.5$ [$M_{\odot} \text{ yr}^{-1}$] this discrepancy can vary between a factor 2 – 10 ([Lee et al. 2009](#)). However, in LITTLE-THINGS galaxies this discrepancy is at most a factor three, which is possibly due to a lack in sensitivity of the $\text{H}\alpha$ measurements ([Hunter et al. 2010](#)). Part of the offset between LITTLE-THINGS galaxies and LSBGs may indicate that these dwarf irregulars have higher SFR than the Local LSBGs of comparable mass. Within this scenario, LSB-D appears to be more similar to the SF dwarf irregulars than to the more quiescent LSBGs, which also tend to live in less dense environments.

When converting the SFR to specific star formation rate (SFR/M_{\star}) we see that while Local Universe galaxies lie around or below the inverse Hubble time relation, they would have reached their current stellar mass with their average sSFR since the Big Bang. LSB-D lies above the relation suggesting that it would have doubled its stellar mass in a Hubble time with its current sSFR (Fig. 9, central panel). Hence, for its stellar mass the current LSB-D’s SFR is too high to have always been on-going. Moreover, the depletion time of its gas reservoir ($t_{\text{dep}} = M_{\text{gas}}/\text{SFR}$) is much smaller than a Hubble time (Fig. 9, bottom panel) indicating that if LSB-D had formed stars at its current rate it would have already consumed all its gas.

3.3. The baryon-to-dark-matter content of LSB-D

The baryon-to-halo mass relation of galaxies (BHMR) is a powerful tool to study the efficiency with which galaxies turn their available baryons into stars and cold gas. In Fig. 10, we place LSB-D on the BHMR and we compare it with expectations based on abundance-matching ([Calette et al. 2021](#)) and against observations of a sample of dwarf and massive nearby disk galaxies spanning five orders of magnitude in baryonic mass from [Mancera Piña et al. \(2022a\)](#). For the latter galaxies the baryon

³ In this analysis we used the same samples of Fig. 9 for which measurements of the SFR and gas and stellar masses were available; SFR for THINGS are taken from [Leroy et al. \(2008\)](#).

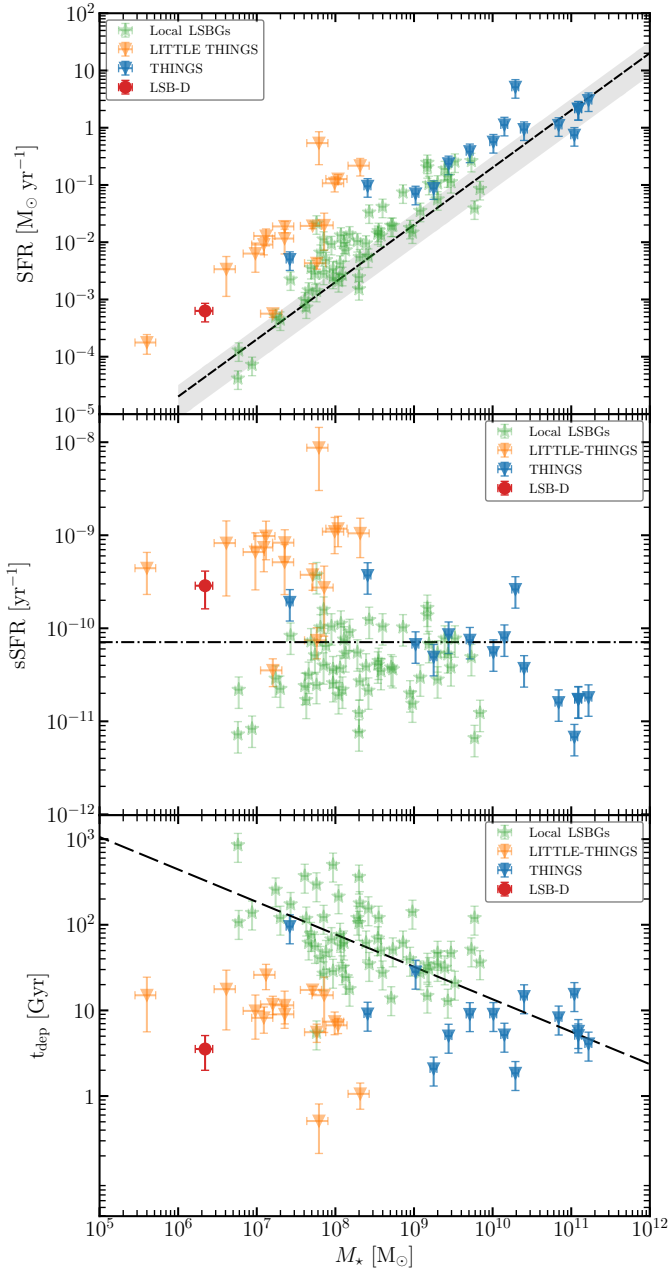


Fig. 9. *Top panel:* star formation rate as a function of stellar mass for LSB-D (marked by the red circle, and for a sample of galaxies in the Local Universe. LITTLE-THINGS (Oh et al. 2015; Iorio et al. 2017) and THINGS galaxies are marked by orange and blue triangles. Local low surface brightness galaxies (LSBGs) from McGaugh (2011), McGaugh et al. (2017) are in green. The dashed line shows a linear relation fitted between the LSBGs and THINGS samples. *Central panel:* specific star formation rate as a function of stellar mass for the same sample as in the top panel. The dashed-dotted line marks the inverse Hubble time, i.e. galaxies on the relation reach their current stellar mass with their average SFR since the Big Bang. *Bottom panel:* depletion time as a function of stellar mass for LSB-D and the samples of galaxies in the Local Universe. The dashed line marks the linear fit relation for the Local LSBGs sample.

fraction⁴ is estimated via accurate mass modelling from their

⁴ f_{bar} , the ratio between their baryonic (M_{bar}) to halo (M_{200}) mass normalized by the cosmological baryon fraction $f_{\text{bar,cosmic}} = 0.16$.

rotation curve decomposition (see Mancera Piña et al. 2022a, for details).

For LSB-D we do not have a rotation curve, so we approximate its approximate location in Fig. 10 as follows. We estimate the circular speed of the galaxy as $v_{\text{circ}} = v_{\text{rot}}$. This means that we ignore corrections for line broadening due to turbulence as well as asymmetric drift (which would decrease and increase our v_{circ} , respectively, e.g. Verheijen 2001; Iorio et al. 2017), which we cannot properly characterize because of the spatial resolution of our observations and considering that both corrections counteract each other. To estimate the uncertainty of v_{circ} we consider the error propagation in v_{rot} (taking into account our error in the measurement in v_{rot} and in the inclination uncertainty), and we add (in quadrature) an additional term of 3 km s^{-1} associated with the asymmetric drift correction based on the typical value of such correction in low-mass systems (e.g. Lelli et al. 2014; Iorio et al. 2017; Mancera Piña et al. 2021). We compare our value of v_{circ} against a set of circular speed profiles of Navarro-Frenk-White (NFW, Navarro et al. 1996) haloes of different halo masses and with concentration parameters following the concentration-mass relation from N -body cosmological simulations (Dutton & Macciò 2014). Given that this relation shows a tail towards low concentrations at low masses (Mancera Piña et al. 2022b; Kong et al. 2022), we also consider NFW profiles with concentration parameters 2σ below the nominal expectation. We find that our estimate of v_{circ} can be matched with the circular speed of a halo of $\sim 10^8 M_{\odot}$. Using this value, we add LSB-D to Fig. 10, though it is worth noticing that the uncertainties in v_{circ} allow for haloes in a broader mass range ($7 \lesssim \log(M_{200}/M_{\odot}) \lesssim 8.75$). LSB-D has baryon-to-halo mass properties similar to dwarf galaxy DDO210 (e.g. LITTLE THINGS, Hunter et al. 2012).

Abundance matching techniques suggest that the BHMR relation steeply and monotonically increases as a function of M_{\star} up to $M_{\text{halo}} \sim 10^{12} M_{\odot}$ (e.g. Moster et al. 2013), but the behaviour at low-masses is only extrapolated from the relation in the 10^9 – $10^{11} M_{\odot}$ range. The properties of LSB-D, along with DDO210, suggest the relation may be flatter, and that low surface brightness galaxies may retain their gas within the dark-matter halo while assembling their stellar content. This agrees with the BHMR relation obtained by Calette et al. (2021) who used both abundance matching to link M_{\star} with M_{200} and empirical correlations to link M_{\star} to M_{gas} , or the relation by Posti et al. (2019) based on HI rotation curve measurements. Alternatively, LSB-D and DDO210 may represent the part of the low-mass population with relatively large baryonic masses for their halo mass, while most of the sources with low baryonic masses are undetected.

LSB-D and DDO210 are two of the few known sources of low-stellar mass for which the stellar-to-mass halo content can be estimated accurately, hence they provide an observational constraint to the low-mass end ($\lesssim 5 \times 10^7 M_{\odot}$) of the stellar-to-mass halo relation. Overall, our analysis on LSB-D adds to the emerging picture of a large scatter in the baryon-content of low-mass galaxies due to feedback from star formation, which modern hydrodynamical simulations should aim to reproduce (McGaugh 2012).

Even though the gravitational potential and the baryon content of LSB-D and DDO210 are similar, their HI properties have some striking differences. First, the minimum HI column density detected in DDO210 is $6 \times 10^{19} \text{ cm}^{-2}$ (which corresponds to a S/N=3 in the moment-zero map; Iorio et al. 2017) and its HI surface brightness profile peaks in the centre at $6 \times 10^{20} \text{ cm}^{-2}$. LSB-D has HI column densities one order of magnitude lower, peaking at $3.3 \times 10^{19} \text{ cm}^{-2}$, and it would have

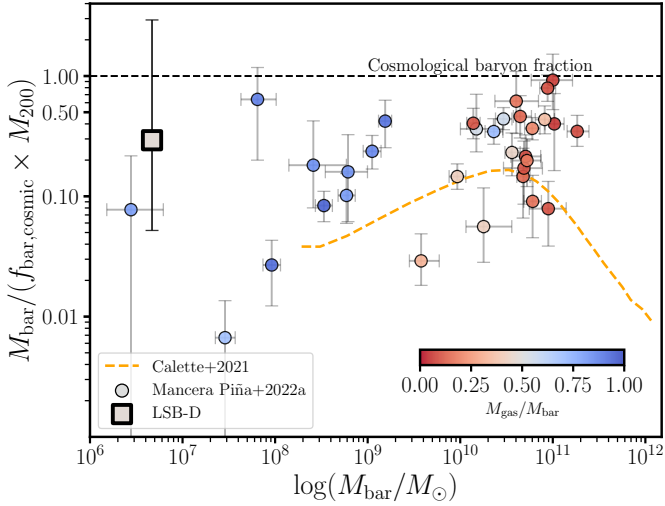


Fig. 10. M_{bar}/M_{200} ratio normalized to the cosmological baryon fraction ($f_{\text{bar,cosmic}}$). LSB-D is compared against a set of nearby disk galaxies (Mancera Piña et al. 2022a) and the semi-empirical relation from Calette et al. (2021), which uses abundance matching to link M_{\star} with M_{200} and empirical correlations for $M_{\text{star}}/M_{\text{gas}}$. Galaxies are colour coded according to their gas-to-baryon content ($M_{\text{gas}}/M_{\text{bar}}$).

been at the detection limit of DDO210’s VLA observations ($N_{\text{HI}}(3\sigma, 4 \text{ km s}^{-1}) = 1.3 \times 10^{19} \text{ cm}^{-2}$; Hunter et al. 2012). Second, LSB-D’s HI disk is much more extended ($r_{\text{HI,LSB-D}} = 1.4 \text{ kpc}$), than the one of DDO210 ($r_{\text{HI,DD0210}} = 0.3 \text{ kpc}$). LSB-D and DDO210 likely had a different formation history, which one disk being much more diffuse than the other. LSB-D appears closer in projection to its massive neighbours than DDO210. In the Local Group, DDO210 and other dwarf galaxies with $M_{\text{HI}} \geq 10^6 M_{\odot}$ are located beyond 300 kpc from the Milky Way or Andromeda. Within 300 kpc dwarf satellites have low amounts of HI ($M_{\text{HI}} \lesssim 10^6 M_{\odot}$) below the detection limit of currently available observations (e.g. Grcevich & Putman 2009; Spekkens et al. 2014), or no HI at all. This also suggest that LSB-D’s interaction with the environment of Dorado, either began recently or has not been sufficiently disruptive to deplete the galaxy of HI.

Different scenarios may explain the absence of galaxies similar to LSB-D close to the Milky Way or Andromeda. Those low surface brightness galaxies may not yet have entered the group (such as DDO210), or they could have already lost their HI because of stronger interactions, or they could exist but because of their low-column density gas ($\lesssim 10^{19} \text{ cm}^{-2}$) they have not yet been detected. Dorado is not the only environment where we find several gas-rich low-mass satellites. Until wide-field HI observations of the LG with comparable sensitivities and resolutions to MHONGOOSE will become available, it will be unclear if the evolution of Milky Way’s satellites is representative of satellites in other groups, as suggested by the Satellites Around Galactic Analogs (SAGA) Survey (Geha et al. 2017), and if they provide a good representation of dwarfs in the local universe (Weisz et al. 2011). Even though the HI of the MW may interfere with the detection of close HI rich satellites which could have low radial velocities and not have yet accreted into the galaxy (Garrison-Kimmel et al. 2014).

3.4. On the enhancement of star formation in LSB-D

LSB-D is one of the few galaxies in the $10^6 M_{\odot}$ stellar and gas mass range known beyond the Local Group. Its overall baryon

and halo properties are typical of the dwarf population, nevertheless it presents two main peculiarities: the HI disk has column densities on average one order of magnitude lower than the HI disks of Local LSBGs ($\sim 10^{18-19} \text{ cm}^{-2}$) and in its centre UV emission indicates recent star formation. Here, we discuss on the possible evolutionary scenarios that shape LSB-D as we see it now.

LSB-D is located in the outskirts of the Dorado group and likely only recently entered in the Dorado group (see Sect. 3.1). Possibly the interaction with the group’s environment is linked to the enhancement of the star formation. With the information available we cannot connect the timescales of the infall to the triggering of the SF, but we can make some considerations on the environmental processes that may have occurred. LSB-D could be the remnant of a tidal interaction that has occurred between NGC 1581 and NGC 1566, but tidal dwarfs usually lack dark matter and the distances and especially relative velocities between LSB-D and these galaxies may suggest this is not the most likely scenario. The tidal interaction nevertheless strongly unsettled the HI disks of the NGC 1581 and NGC 1566. Several HI streams and clouds are found around both galaxies (Fig. 1). In between NGC 1581 and LSB-D (at 45 projected-kpc from the latter) an HI cloud is visible at the detection limit of our observations (see Sect. 2.1 and Fig. B.1) with small relative velocity to LSB-D ($\Delta v = 78 \text{ km s}^{-1}$). The location of LSB-D on the BHMR (Sect. 3.3) suggests that the galaxy has a high fraction of baryons in its halo, $\sim 50\%$ of which are in the gas phase. It is possible that while entering the group, LSB-D caught in its halo part of the HI clouds remnant of the interaction. This HI is now condensing onto the irregular disk we see now. This would explain why the disk may not fully rotating, the higher HI line-width in the centre and the extended tail in the NW may be traces of this condensation. While condensing, part of the HI in the centre may have triggered a new episode of SF. Nevertheless, very little is known about the evolution of these low-mass systems, numerical simulations have also shown that HI disks of this mass can be retained by the galaxy’s halo and re-settle in a rotating disk triggering a new episode of star-formation (Rey et al. 2024). In this picture, LSB-D could also have retained its HI within its disk over cosmic time and we are seeing a phase of re-settlement and condensation of its disk.

Even though the origin of LSB-D’s HI disk is unclear, different indications predict that it will be short-lived. Star formation feedback can disrupt an HI disk similar to LSB-D in a few hundred Myr (Rey et al. 2024), and the interaction with the intergalactic medium can also strip the gas off the galaxy. While most common in the dense environment of clusters, also in groups and the field ram pressure (RP) can be an efficient hydro-dynamical mechanism to strip galaxies (e.g. Poggianti et al. 2017; Vulcani et al. 2021). RP is likely removing HI from dwarf MW satellites and in the Sculptor group (Westmeier et al. 2011, 2015), possibly triggering SF in the dwarf galaxies Pegasus, Wolf-Lundmark-Melotte and Holmberg II in the outskirts ($\sim 900 \text{ kpc}$) of the LG and M81 groups (e.g. McConnachie et al. 2007; Ianjamasimanana et al. 2020; Yang et al. 2022; Bureau & Carignan 2002). In the Fornax and Virgo clusters, RP could have depleted of their gas dwarf galaxies with similar dynamical masses to LSB-D (Boselli et al. 2008a; Venhola et al. 2022; Kleiner et al. 2023; Boselli et al. 2023). This would explain the abundance of dwarf gas poor ellipticals compared to other types of galaxies (e.g. Boselli et al. 2008b; Venhola et al. 2022). Interestingly, Dorado has tens of known low surface brightness galaxies within 150 projected-kpc from the two central galaxies (Carrasco et al. 2001). None are

known to have gas, and the two that were in the MeerKAT field of view had no detectable HI. This may suggest that the hydrodynamical interaction with the intra-group medium of Dorado has an effect on its low-mass members.

RP may already be shaping the HI disk of LSB-D. Ram pressure exerted by the IGM would explain the offset HI disk with respect to the optical body, its elongated tail in the direction opposite of infall, and possibly the recent enhancement of the SF. RP is efficient when the pressure (P_{RP}) exerted by the IGM on a galaxy moving at a relative velocity, v , overcomes the pressure imposed on the gas disk by a galaxy's own gravitational potential (P_{grav} , e.g. Gunn et al. 1972):

$$P_{\text{RP}} = \rho_{\text{IGM}} v^2 \gtrsim 2\pi G \Sigma_{\text{tot}} \Sigma_{\text{gas}} \approx P_{\text{grav}} \quad (4)$$

where ρ_{IGM} is the IGM density, given by the product of the number of atoms in the IGM and the mean mass of a particle in the ionised medium, $\mu = 0.75 m_p$, $\Sigma_{\text{tot}} = M_{\text{tot}} / (\pi R_{\text{tot}}^2)$ is the total surface density (stars plus gas) and Σ_{gas} is the ISM surface density of the disk. At the outermost edge of LSB-D's disk ($r_{\text{HI}} = 2.1$ kpc), the gas has column density of $2.8 \times 10^{18} \text{ cm}^{-2}$, which corresponds to $\Sigma_{\text{HI}} = 0.022 M_{\odot} \text{ pc}^{-2}$. Correcting for helium abundance we obtain $\Sigma_{\text{gas}} = 0.029 M_{\odot} \text{ pc}^{-2}$. As illustrated in Sect. 3.2, the total baryonic mass of LSB-D is $M_{\text{tot}} = M_{\text{bar}} = 4.43 \times 10^6 M_{\odot}$. Hence, ram pressure would be effective on LSB-D if it was greater than $P_{\text{RP}} \gtrsim 2.9 \times 10^{-15} \text{ dyn cm}^{-2}$.

In Sect. 3.1 we estimated the median deprojected velocity LSB-D's velocity of LSB-D based on a set of N -body simulation of satellites within a Dorado-like group, ($v = 509_{-242}^{208} \text{ km s}^{-1}$). Assuming this velocity, for RP to take effect onto LSB-D the IGM of Dorado would have to have densities $n_{\text{IGM}} = \rho_{\text{IGM}} \gtrsim 3 \times 10^{-7} \text{ cm}^{-3}$. In these low density environments (similar to the outskirts of Virgo, Steyrleithner et al. 2020) RP has been observed to efficiently strip the gas off low HI mass galaxies (e.g. Westmeier et al. 2015; Ramatsoku et al. 2019; Boselli et al. 2023), hence is possible that also in Dorado ram-pressure from the IGM is shaping the HI disk of LSB-D.

Ram-pressure may enhance star-formation in the disks and in the stripped tails of galaxies (Poggianti et al. 2017; Vulcani et al. 2018), however beyond the Local Universe this mechanism has only been observed in galaxies of masses $M_{\star} \gtrsim 10^9 M_{\odot}$ (Boselli et al. 2008b; Fritz et al. 2017). In the outskirts of the Virgo cluster ($8 \times 10^{-5} \lesssim n_{\text{IGM}} \lesssim 10^{-7} \text{ atoms cm}^{-3}$), simulations have shown that SF can be caused by RP in galaxies with similar masses to LSB-D ($M_{\text{bar}} = 10^6 M_{\odot}$, $M_{\text{DM}} = 10^8 M_{\odot}$) travelling through the medium with velocities as low as 200 km s^{-1} (Steyrleithner et al. 2020). Similarly, in the MW halo's outskirts RP of the same order of magnitudes ($\gtrsim 10^{-15} \text{ dyn cm}^{-2}$) may trigger SF in low-mass satellites (Samuel et al. 2023). Possibly, the same phenomenon is on-going in LSB-D. If that were the case, it would be the first time that this phenomenon is observed in a source of this low dynamical mass in the outskirts of a low-density group, like Dorado. Stripping must have, nevertheless, only just recently begun, otherwise in a few tens Myr the galaxy would have likely lost its HI, as is observed in the low-mass Fornax cluster (Kleiner et al. 2023). This also highlights the short-lived fate of LSB-D's HI disk.

4. Conclusions and future prospects

In this paper we presented deep new MeerKAT 21-cm observations of the field of NGC 1566 from MHONGOOSE, which led to the discovery of the gas-rich LSBG LSB-D in the Dorado

group. Combining the HI observations with deep optical images from VEGAS we determined the HI and stellar properties of one of the lowest-mass HI-rich galaxies thus far known outside the Local Group ($M_{\text{bar}} = M_{\text{gas}} + M_{\star} = 4.43 \times 10^6 M_{\odot}$, $f_{\text{gas}} = 0.48$, Sect. 2.1). The HI disk has low column densities, the gas is compressed in the southern edge, and has an outer asymmetry in the opposite direction. Overall, the disk is likely supported by rotation. In the centre, where the HI line-width is higher ($\sigma = 5.5 \text{ km s}^{-1}$, Sect. 2.2), the stellar body has bluer colours and coincident UV emission indicates on-going star formation (Sect. 2.3). The SFR of LSB-D is similar to that of star-forming dwarf galaxies in the Local Group.

The gas and stellar properties of LSB-D allow us to draw a picture of its evolution within Dorado. In the past, LSB-D likely had a first episode of star formation that shaped the stellar body as we see it now. During this episode and throughout the subsequent evolution through cosmic time, LSB-D retained a high percentage of baryons and in particular HI within the halo or this gas was accreted onto its halo, as is indicated by its gas fraction and baryon-to-halo mass content (see Fig. 10). Possibly, the HI disk has not been consumed by further star formation because its column densities are too low for the gas to cool into dense molecular clouds and generate a new episode of star formation (Kanekar et al. 2011; Maccagni et al. 2017). LSB-D evolved mostly unperturbed until recent times, when it began its first infall into the Dorado group (Sect. 3.1). During its infall, LSB-D did not have a major interaction with other nearby galaxies but likely the environment caused the formation of the HI disk and the recent enhancement of SF. In Sect. 3.4, we suggested that on the one hand, the orbit within the group may have caused the HI in the halo to condense in the disk, and start a new epoch of star formation, or LSB-D may have caught some sparse HI clouds from Dorado's IGM which are now forming a disk, and stars. On the other hand, RP from the low-density IGM may also be stripping the HI disk, while compressing it in the centre and possibly triggering the new episode of SF (Sect. 3.4). In all scenarios, LSB-D's HI disk will likely be short-lived and survive only a few hundred million years.

In the future, Integral Field Unit observations in the optical band may be able to shed new light on the star formation history of LSB-D and provide information on its stellar kinematics. The high-resolution ($\lesssim 1''$) study of the stellar body of LSB-D (and of its kinematics with respect to the HI), as well as of its ionised gas and chemical composition, will enable us to obtain a precise measurement of its star formation rate, determine which phenomena affect its multi-phase ISM, and study its evolution within Dorado.

Given its very low mass, the discovery of LSB-D beyond the Local Group, and the detailed study of its HI and stellar properties, demonstrates that the combination of MHONGOOSE observations with deep optical images opens a new parameter space of studies of LSBGs. In the observations presented in this paper, four other sources with HI mass lower than $2 \times 10^7 M_{\odot}$ have also been detected in the proximity of NGC 1566. MHONGOOSE is observing $\approx 24 \text{ deg}^2$ with high sensitivity to low-density gas and low HI masses, and is commensally observing the same fields with the VST with high-surface-brightness sensitivities. This will enable the discovery and detailed analysis of several more low-mass gas-rich galaxies in the field environment. The first data release (DR1, with five hours of observing time per target, $\sqrt{10}$ less sensitive than the observations shown in this paper) already discovered five new sources (de Blok et al. 2024), amongst the 46 additional HI satellites detected around its targets. The full survey with ten times the observing time of

MHONGOOSE-DR1 will certainly discover more objects like LSB-D.

The studies of ultra-low-mass HI rich galaxies have so far been limited to the Local Group, which alone cannot provide a representative picture of the evolution of dwarf galaxies. The study of LSB-D, and the many more that will be discovered in the future, will make possible Local Group cosmological studies in different environments in the nearby Universe. Extending the study done on LSB-D to all newly discovered sources will allow us to populate the low-mass end of the BHMR and study the scatter (and its origin) in the BTF relation. Moreover, these studies enable a direct comparison with the kinematics, gas content, and environmental effects of dwarf satellite galaxies present in large-volume hydrodynamical simulations (Rohr et al. 2023; Samuel et al. 2023; Jones et al. 2024), which will quantify the main differences between the observed and simulated galaxy assembly processes, thus enabling us to provide observational constraints for a more detailed description of these phenomena in the next generation of simulations.

Acknowledgements. The authors thank the anonymous referee for the useful comments and suggestions. We thank Dr. Teymoor Saifollahi for giving the suggestion to write this paper. This project has received funding from the European Research Council (ERC) under the European Union's Horizon 2020 research and innovation programme (grant agreement no. 882793). PEMP acknowledges the support from the Dutch Research Council (NWO) through the Veni grant VI.Veni.222.364 KAO acknowledges support by the Royal Society through a Dorothy Hodgkin Fellowship (DHF\R1\231105) and by STFC through grant ST/T000244/1. This work used the DiRAC@Durham facility managed by the Institute for Computational Cosmology on behalf of the STFC DiRAC HPC Facility (www.dirac.ac.uk). The equipment was funded by BEIS capital funding via STFC capital grants ST/K00042X/1, ST/P002293/1, ST/R002371/1 and ST/S002502/1, Durham University and STFC operations grant ST/R000832/1. DiRAC is part of the National e-Infrastructure. AB acknowledges support from the Centre National d'Etudes Spatial (CNES), France. MK acknowledges support from the National Research Foundation of Korea (NRF) grant funded by the Korea government (Ministry of Science and ICT: MSIT) (No. NRF-RS-2023-00243222, NRF-RS-2022-00197685). This paper makes use of MeerKAT data. The MeerKAT telescope is operated by the South African Radio Astronomy Observatory, which is a facility of the National Research Foundation, an agency of the Department of Science and Innovation. (Part of) the data published here have been reduced using the CARACal pipeline, partially supported by ERC Starting grant number 679627 "FORNAX", MAECI Grant Number ZA18GR02, DST-NRF Grant Number 113121 as part of the ISARP Joint Research Scheme, and BMBF project 05A17PC2 for D-MeerKAT. Information about CARACal can be obtained online under the URL: <https://caracal.readthedocs.io>.

References

Adams, E. A. K., & Oosterloo, T. A. 2018, *A&A*, 612, A26
 Adams, E. A. K., Adebahr, B., de Blok, W. J. G., et al. 2022, *A&A*, 667, A38
 Anand, G. S., Lee, J. C., Van Dyk, S. D., et al. 2021, *MNRAS*, 501, 3621
 Begum, A., Chengalur, J. N., Karachentsev, I. D., & Sharina, M. E. 2008, *MNRAS*, 386, 138
 Bernstein-Cooper, E. Z., Cannon, J. M., Elson, E. C., et al. 2014, *AJ*, 148, 35
 Bianchi, L., & Garcia, M. 2014, *Adv. Space Res.*, 53, 973
 Boselli, A., Boissier, S., Cortese, L., & Gavazzi, G. 2008a, *ApJ*, 674, 742
 Boselli, A., Boissier, S., Cortese, L., & Gavazzi, G. 2008b, *A&A*, 489, 1015
 Boselli, A., Serra, P., de Gasperin, F., et al. 2023, *A&A*, 676, A92
 Bosma, A. 1978, PhD Thesis, University of Groningen, The Netherlands
 Bouchard, A., Carignan, C., & Staveley-Smith, L. 2006, *AJ*, 131, 2913
 Briggs, D. S., Schwab, F. R., & Sramek, R. A. 1999, *ASP Conf. Ser.*, 180, 127
 Buck, T., Macciò, A. V., Dutton, A. A., Obreja, A., & Frings, J. 2019, *MNRAS*, 483, 1314
 Bureau, M., & Carignan, C. 2002, *AJ*, 123, 1316
 Calette, A. R., Rodríguez-Puebla, A., Avila-Reese, V., Lagos, C., & d. P., 2021, *MNRAS*, 506, 1507
 Camilo, F., Scholz, P., Serylak, M., et al. 2018, *ApJ*, 856, 180
 Capaccioli, M., Spavone, M., Grado, A., et al. 2015, *A&A*, 581, A10
 Carrasco, E. R., Mendes de Oliveira, C., Infante, L., & Bolte, M. 2001, *AJ*, 121, 148

Das, M., McGaugh, S. S., Ianjamasimanana, R., Schombert, J., & Dwarakanath, K. S. 2020, *ApJ*, 889, 10
 de Blok, W. J. G., Adams, E. A. K., Amram, P., et al. 2016, *MeerKAT Science: On the Pathway to the SKA*, 7
 de Blok, W. J. G., Athanassoula, E., Bosma, A., et al. 2020, *A&A*, 643, A147
 de Blok, W. J. G., Healy, J., Maccagni, F. M., et al. 2024, *A&A*, 688, A109
 Dey, A., Schlegel, D. J., Lang, D., et al. 2019, *AJ*, 157, 168
 Duc, P. A., & Mirabel, I. F. 1998, *A&A*, 333, 813
 Dutton, A. A., & Macciò, A. V. 2014, *MNRAS*, 441, 3359
 Elagali, A., Staveley-Smith, L., Rhee, J., et al. 2019, *MNRAS*, 487, 2797
 Firth, P., Evstigneeva, E. A., Jones, J. B., et al. 2006, *MNRAS*, 372, 1856
 Forbes, D. A., Dullo, B. T., Gannon, J., et al. 2020, *MNRAS*, 494, 5293
 Fritz, J., Moretti, A., Gullieuszik, M., et al. 2017, *ApJ*, 848, 132
 Garrison-Kimmel, S., Boylan-Kolchin, M., Bullock, J. S., & Lee, K. 2014, *MNRAS*, 438, 2578
 Geha, M., Blanton, M. R., Masjedi, M., & West, A. A. 2006, *ApJ*, 653, 240
 Geha, M., Wechsler, R. H., Mao, Y.-Y., et al. 2017, *ApJ*, 847, 4
 Gil de Paz, A., Boissier, S., Madore, B. F., et al. 2007, *ApJS*, 173, 185
 Giovanelli, R., Haynes, M. P., Adams, E. A. K., et al. 2013, *AJ*, 146, 15
 Gray, L. M., Rhode, K. L., Leisman, L., et al. 2023, *AJ*, 165, 197
 Greivich, J., & Putman, M. E. 2009, *ApJ*, 696, 385
 Gunn, J. E., Gott, J., & Richard, I. 1972, *ApJ*, 176, 1
 Honey, M., van Driel, W., Das, M., & Martin, J. M. 2018, *MNRAS*, 476, 4488
 Hunter, D. A., Elmegreen, B. G., & Ludka, B. C. 2010, *AJ*, 139, 447
 Hunter, D. A., Ficut-Vicas, D., Ashley, T., et al. 2012, *AJ*, 144, 134
 Ianjamasimanana, R., Namumba, B., Ramaila, A. J. T., et al. 2020, *MNRAS*, 497, 4795
 Into, T., & Portinari, L. 2013, *MNRAS*, 430, 2715
 Iodice, E., Cantiello, M., Hilker, M., et al. 2020, *A&A*, 642, A48
 Iodice, E., Spavone, M., Raj, M. A., et al. 2021, *ArXiv e-prints* [arXiv:2102.04950]
 Iorio, G., Fraternali, F., Nipoti, C., et al. 2017, *MNRAS*, 466, 4159
 Jaffé, Y. L., Smith, R., Candlish, G. N., et al. 2015, *MNRAS*, 448, 1715
 Jarrett, T. H., Comrie, A., Marchetti, L., et al. 2021, *Astron. Comput.*, 37, 100502
 Jones, M. G., Sand, D. J., Karunakaran, A., et al. 2024, *ApJ*, 966, 93
 Józsa, G. I. G., White, S. V., Thorat, K., et al. 2020, *ASP Conf. Ser.*, 527, 635
 Józsa, G. I. G., Thorat, K., Kamphuis, P., et al. 2021, *MNRAS*, 501, 2704
 Kanekar, N., Braun, R., & Roy, N. 2011, *ApJ*, 737, L33
 Kilborn, V. A., Koribalski, B. S., Forbes, D. A., Barnes, D. G., & Musgrave, R. C. 2005, *MNRAS*, 356, 77
 Kleiner, D., Serra, P., Maccagni, F. M., et al. 2023, *A&A*, 675, A108
 Kong, D., Kaplinghat, M., Yu, H.-B., Fraternali, F., & Mancera Piña, P. E. 2022, *ApJ*, 936, 166
 Koribalski, B. S., Wang, J., Kamphuis, P., et al. 2018, *MNRAS*, 478, 1611
 Kourkchi, E., & Tully, R. B. 2017, *ApJ*, 843, 16
 Kuijken, K. 2011, *The Messenger*, 146, 8
 Lee, J. C., de Paz, A. G., Tremonti, C., et al. 2009, *ApJ*, 706, 599
 Leisman, L., Haynes, M. P., Janowiecki, S., et al. 2017, *ApJ*, 842, 133
 Lelli, F. 2022, *Nat. Astron.*, 6, 35
 Lelli, F., Verheijen, M., & Fraternali, F. 2014, *A&A*, 566, A71
 Lelli, F., McGaugh, S. S., & Schombert, J. M. 2016, *AJ*, 152, 157
 Lelli, F., McGaugh, S. S., Schombert, J. M., Desmond, H., & Katz, H. 2019, *MNRAS*, 484, 3267
 Leroy, A. K., Walter, F., Brinks, E., et al. 2008, *AJ*, 136, 2782
 Leroy, A. K., Sandstrom, K. M., Lang, D., et al. 2019, *ApJS*, 244, 24
 Maccagni, F. M., Morganti, R., Oosterloo, T. A., Geréb, K., & Maddox, N. 2017, *A&A*, 604, A43
 Maccagni, F. M., Ruffa, I., Loni, A., et al. 2023, *A&A*, 675, A59
 Mancera Piña, P. E., Fraternali, F., Adams, E. A. K., et al. 2019, *ApJ*, 883, L33
 Mancera Piña, P. E., Posti, L., Fraternali, F., Adams, E. A. K., & Oosterloo, T. 2021, *A&A*, 647, A76
 Mancera Piña, P. E., Fraternali, F., Oosterloo, T., et al. 2022a, *MNRAS*, 514, 3329
 Mancera Piña, P. E., Fraternali, F., Oosterloo, T., et al. 2022b, *MNRAS*, 512, 3230
 Marasco, A., Belfiore, F., Cresci, G., et al. 2023, *A&A*, 670, A92
 Martínez-Delgado, D., Cooper, A. P., Román, J., et al. 2023, *A&A*, 671, A141
 Mauch, T., Cotton, W. D., Condon, J. J., et al. 2020, *ApJ*, 888, 61
 McConnachie, A. W., Venn, K. A., Irwin, M. J., Young, L. M., & Geehan, J. J. 2007, *ApJ*, 671, L33
 McFarland, J. P., Verdoes-Kleijn, G., Sikkema, G., et al. 2013, *Exp. Astron.*, 35, 45
 McGaugh, S. S. 2011, *Phys. Rev. Lett.*, 106, 121303
 McGaugh, S. S. 2012, *AJ*, 143, 40
 McGaugh, S. S., Schombert, J. M., Bothun, G. D., & de Blok, W. J. G. 2000, *ApJ*, 533, L99
 McGaugh, S. S., Schombert, J. M., & Lelli, F. 2017, *ApJ*, 851, 22

- McGaugh, S. S., Lelli, F., Schombert, J. M., et al. 2021, *AJ*, **162**, 202
- McQuinn, K. B. W., Mitchell, N. P., & Skillman, E. D. 2015a, *ApJS*, **218**, 29
- McQuinn, K. B. W., Skillman, E. D., Dolphin, A. E., & Mitchell, N. P. 2015b, *ApJ*, **808**, 109
- Meyer, M., Robotham, A., Obreschkow, D., et al. 2017, *PASA*, **34**, 52
- Moster, B. P., Naab, T., & White, S. D. M. 2013, *MNRAS*, **428**, 3121
- Navarro, J. F., Frenk, C. S., & White, S. D. M. 1996, *ApJ*, **462**, 563
- Navarro, J. F., Frenk, C. S., & White, S. D. M. 1997, *ApJ*, **490**, 493
- Oh, S. H., Kim, W.-T., & Lee, H. M. 2015, *ApJ*, **807**, 73
- Oman, K. A., Hudson, M. J., & Behroozi, P. S. 2013, *MNRAS*, **431**, 2307
- Oman, K. A., Bahé, Y. M., Healy, J., et al. 2021, *MNRAS*, **501**, 5073
- Ott, J., Stilp, A. M., Warren, S. R., et al. 2012, *AJ*, **144**, 123
- Planck Collaboration VI. 2020, *A&A*, **641**, A6
- Poggianti, B. M., Moretti, A., Gullieuszik, M., et al. 2017, *ApJ*, **844**, 48
- Ponomareva, A. A., Verheijen, M. A. W., Papastergis, E., Bosma, A., & Peletier, R. F. 2018, *MNRAS*, **474**, 4366
- Posti, L., Fraternali, F., & Marasco, A. 2019, *A&A*, **626**, A56
- Ragusa, R., Spavone, M., Iodice, E., et al. 2021, *A&A*, **651**, A39
- Ragusa, R., Mirabile, M., Spavone, M., et al. 2022, *Front. Astron. Space Sci.*, **9**, 852810
- Ragusa, R., Iodice, E., Spavone, M., et al. 2023, *A&A*, **670**, L20
- Ramatsozku, M., Serra, P., Poggianti, B. M., et al. 2019, *MNRAS*, **487**, 4580
- Rampazzo, R., Ciroi, S., Mazzei, P., et al. 2020, *A&A*, **643**, A176
- Rampazzo, R., Mazzei, P., Marino, A., et al. 2021, *JAA*, **42**, 31
- Rampazzo, R., Mazzei, P., Marino, A., et al. 2022, *A&A*, **664**, A192
- Read, J. I., Iorio, G., Agertz, O., & Fraternali, F. 2017, *MNRAS*, **467**, 2019
- Rey, M. P., Orkney, M. D. A., Read, J. I., et al. 2024, *MNRAS*, **529**, 2379
- Rhee, J., Smith, R., Choi, H., et al. 2017, *ApJ*, **843**, 128
- Rohr, E., Pillepich, A., Nelson, D., et al. 2023, *MNRAS*, **524**, 3502
- Ryan-Weber, E. V., Begum, A., Oosterloo, T., et al. 2008, *MNRAS*, **384**, 535
- Sakai, S., Mould, J. R., Hughes, S. M. G., et al. 2000, *ApJ*, **529**, 698
- Salim, S., Rich, R. M., Charlot, S., et al. 2007, *ApJS*, **173**, 267
- Samuel, J., Padasani, B., Wetzel, A., et al. 2023, *MNRAS*, **525**, 3849
- Sancisi, R., Fraternali, F., Oosterloo, T., & van der Hulst, T. 2008, *A&A Rev.*, **15**, 189
- Schaye, J., Crain, R. A., Bower, R. G., et al. 2015, *MNRAS*, **446**, 521
- Schlafly, E. F., & Finkbeiner, D. P. 2011, *ApJ*, **737**, 103
- Serra, P., Westmeier, T., Giese, N., et al. 2015, *MNRAS*, **448**, 1922
- Serra, P., Maccagni, F. M., Kleiner, D., et al. 2019, *A&A*, **628**, A122
- Serra, P., Maccagni, F. M., Kleiner, D., et al. 2023, *A&A*, **673**, A146
- Spavone, M., Capaccioli, M., Napolitano, N. R., et al. 2017, *A&A*, **603**, A38
- Spekkens, K., Urbancic, N., Mason, B. S., Willman, B., & Aguirre, J. E. 2014, *ApJ*, **795**, L5
- Steyrleithner, P., Hensler, G., & Boselli, A. 2020, *MNRAS*, **494**, 1114
- Swaters, R. A., van Albada, T. S., van der Hulst, J. M., & Sancisi, R. 2002, *A&A*, **390**, 829
- Tanoglidis, D., Drlica-Wagner, A., Wei, K., et al. 2021, *ApJS*, **252**, 18
- Venhola, A., Peletier, R., Laurikainen, E., et al. 2017, *A&A*, **608**, A142
- Venhola, A., Peletier, R. F., Salo, H., et al. 2022, *A&A*, **662**, A43
- Verheijen, M. A. W. 2001, *ApJ*, **563**, 694
- Vulcani, B., Poggianti, B. M., Gullieuszik, M., et al. 2018, *ApJ*, **866**, L25
- Vulcani, B., Poggianti, B. M., Moretti, A., et al. 2021, *ApJ*, **914**, 27
- Wall, R. E., Kilic, M., Bergeron, P., et al. 2019, *MNRAS*, **489**, 5046
- Walter, F., Brinks, E., de Blok, W. J. G., et al. 2008, *AJ*, **136**, 2563
- Warren, S. R., Skillman, E. D., Stilp, A. M., et al. 2012, *ApJ*, **757**, 84
- Weisz, D. R., Dolphin, A. E., Dalcanton, J. J., et al. 2011, *ApJ*, **743**, 8
- Westmeier, T., Braun, R., & Koribalski, B. S. 2011, *MNRAS*, **410**, 2217
- Westmeier, T., Staveley-Smith, L., Calabretta, M., et al. 2015, *MNRAS*, **453**, 338
- Westmeier, T., Kitaef, S., Pallot, D., et al. 2021, *MNRAS*, **506**, 3962
- Westmeier, T., Deg, N., Spekkens, K., et al. 2022, *PASA*, **39**, e058
- Xu, J.-L., Zhu, M., Yu, N., et al. 2023, *ApJ*, **944**, L40
- Yang, Y., Ianjamasimanana, R., Hammer, F., et al. 2022, *A&A*, **660**, L11
- Young, L. M., van Zee, L., Lo, K. Y., Dohm-Palmer, R. C., & Beierle, M. E. 2003, *ApJ*, **592**, 111
-
- ¹ ASTRON – Netherlands Institute for Radio Astronomy, Oude Hoogeveensedijk 4, 7991 PD Dwingeloo, The Netherlands
- ² INAF – Osservatorio Astronomico di Cagliari, via della Scienza 5, 09047 Selargius (CA), Italy
- ³ Dept. of Astronomy, Univ. of Cape Town, Private Bag X3, Rondebosch 7701, South Africa
- ⁴ Kapteyn Astronomical Institute, University of Groningen, PO Box 800, 9700 AV Groningen, The Netherlands
- ⁵ Leiden Observatory, Leiden University, PO Box 9513, 2300 RA Leiden, The Netherlands
- ⁶ INAF – Osservatorio Astronomico di Capodimonte, via Moiarielelo 16, Napoli 80131, Italy
- ⁷ Department of Astronomy, Case Western Reserve University, Cleveland, OH 44106, USA
- ⁸ Institute for Computational Cosmology, Durham University, South Road, Durham DH1 3LE, United Kingdom
- ⁹ Centre for Extragalactic Astronomy, Durham University, South Road, Durham DH1 3LE, United Kingdom
- ¹⁰ Department of Physics, Durham University, South Road, Durham DH1 3LE, United Kingdom
- ¹¹ Australia Telescope National Facility, CSIRO Astronomy and Space Science, PO Box 76, Epping, NSW 1710, Australia
- ¹² Western Sydney University, Locked Bag 1797, Penrith South, NSW 1797, Australia
- ¹³ Department of Astronomy and Space Science, Sejong University, Seoul 05006, Korea
- ¹⁴ Aix Marseille Univ, CNRS, CNES, LAM, Marseille, France
- ¹⁵ Argelander-Institut für Astronomie, Auf dem Hügel 71, 53121 Bonn, Germany
- ¹⁶ Centre for Astrophysics Research, University of Hertfordshire, College Lane, Hatfield AL10 9AB, UK
- ¹⁷ Instituto de Astrofísica, Departamento de Ciencias Físicas, Universidad Andrés Bello, Fernández Concha 700, Las Condes, Santiago, Chile
- ¹⁸ LERMA, Observatoire de Paris, PSL research Université, CNRS, Sorbonne Université, 75104 Paris, France
- ¹⁹ Collège de France, 11 Place Marcelin Berthelot, 75005 Paris, France
- ²⁰ E.A. Milne Centre for Astrophysics, University of Hull, Hull HU6 7RX, United Kingdom
- ²¹ University of Louisville, Department of Physics and Astronomy, 102 Natural Science Building, 40292, KY Louisville, USA
- ²² Max-Planck-Institut für Radioastronomie, Auf dem Hügel 69, 53121 Bonn, Germany
- ²³ Department of Physics and Electronics, Rhodes University, PO Box 94, Makhanda 6140, South Africa
- ²⁴ Ruhr University Bochum, Faculty of Physics and Astronomy, Astronomical Institute (AIRUB), 44780 Bochum, Germany
- ²⁵ INAF – Padova Astronomical Observatory, Vicolo dell’Osservatorio 5, 35122 Padova, Italy
- ²⁶ Department of Physics and Space Science, Royal Military College of Canada, PO Box 17000, Station Forces Kingston, ON K7K 7B4, Canada
- ²⁷ Department of Physics, Engineering Physics and Astronomy, Queen’s University, Kingston, ON K7L 3N6, Canada
- ²⁸ Max-Planck-Institut für Astronomie, Königstuhl 17, 69117 Heidelberg, Germany
- ²⁹ Department of Physics and Astronomy, The University of Manchester, Manchester M13 9PL, UK

Appendix A: MHONGOOSE datacubes sensitivities and H I detections in Dorado

As mentioned in Sect. 2, we have identified six optimal weighting and tapering combinations that span the resolution range of MeerKAT (7''–90'') at optimal sensitivities with which we generate the H I datacubes. The lowest resolution datacube (94''×92'') is generated with Briggs *robust* = 1.0 and taper to 90'', hence is named **r10_t90**. With *robust* = 0.5 and 60'' tapering we reach 65''×64'' resolution (**r05_t60**). Higher resolution datacubes are generated with different robust weights (*robust* = 1.5, 1.0, 0.5, 0.0) and no tapering reaching resolutions of 32''×23''(r15), 25''×23'' (r10), 12''×10'' (r05) and

7.6''×7.2'' (r00). The noise level matches the expected theoretical values, as illustrated in the survey paper (de Blok et al. 2024). The 3σ H I column density sensitivities in the centre of the cube are computed over 16 km s^{-1} and vary between $5 \times 10^{17} \text{ cm}^{-2}$ at 90'' resolution and $5 \times 10^{19} \text{ cm}^{-2}$ at 7'', for emission filling the beam uniformly. Figure A.1 shows the overlay of the H I flux density maps derived from the datacubes at all resolutions. New H I detections are marked in green.

Table A.1 summarizes the main properties of the datacubes. The datacube used to study LSB-D's H I disk is **r10**, marked in bold in the Table. A summary of the H I properties of the sources detected by the MHONGOOSE observations is given in Table A.2.

Table A.1. Properties of the MHONGOOSE H I datacubes of NGC 1566

Name	Robust/taper	Beam [arcsec]	Noise (1σ) [mJy beam $^{-1}$]	$N_{\text{HI}} 3\sigma, 16 \text{ km s}^{-1}$ [10^{18} cm^{-2}]	S/N = 3 [10^{18} cm^{-2}]
r10_t90	<i>r</i> = 1.0 taper 90''	94 × 92	0.35	0.55	0.61
r05_t60	<i>r</i> = 0.5 taper 60''	72 × 69	0.27	0.74	1.3
r15	<i>r</i> = 1.5	32 × 23	0.16	2.9	3.9
r10	<i>r</i> = 1.0	25 × 18	0.16	4.9	7.7
r05	<i>r</i> = 0.5	12 × 10	0.18	19	21
r00	<i>r</i> = 0.0	7.6 × 7.2	0.22	51	60

Table A.2. H I properties of the sources detected by MHONGOOSE in Dorado.

Name	Coordinates (J2000)	v_{sys} [km s $^{-1}$]	F_{int} [mJy km s $^{-1}$]	M_{HI}^{\dagger} [M_{\odot}]	$w50$ [km s $^{-1}$]
PGC 128826*	04 ^h 16 ^m 17 ^s – 54 ^d 53 ^m 38 ^s	1234	92.8	6.19×10^6	84.0
PGC 075137*	04 ^h 20 ^m 26 ^s – 54 ^d 44 ^m 25 ^s	1336	251	1.82×10^7	64.2
NGC 1566	04 ^h 20 ^m 42 ^s – 54 ^d 56 ^m 16 ^s	1496	165×10^3	1.94×10^{10}	199
MKT 042200-545440*	04 ^h 22 ^m 00 ^s – 54 ^d 54 ^m 40 ^s	1439	170	1.23×10^7	29.2
MKT 042230-550757*	04 ^h 22 ^m 30 ^s – 55 ^d 07 ^m 57 ^s	1335	34.2	2.49×10^6	14.0
MKT 042231-551202**	04 ^h 22 ^m 31 ^s – 55 ^d 12 ^m 02 ^s	1292	5.01	3.65×10^5	10.0
MKT 042326-551621*, LSB-D	04 ^h 23 ^m 26 ^s – 55 ^d 16 ^m 21 ^s	1214	22.9	1.60×10^6	11.4
NGC 1581	04 ^h 24 ^m 44 ^s – 54 ^d 56 ^m 31 ^s	1609	1.38×10^3	1.09×10^8	218

Notes. (*) New H I detections made by MHONGOOSE. (**) H I detection with $S/N = 3$ without an optical counterpart. (\dagger) H I masses are computed at the distance of NGC 1566, $D = 17.69 \text{ Mpc}$ (Anand et al. 2021).

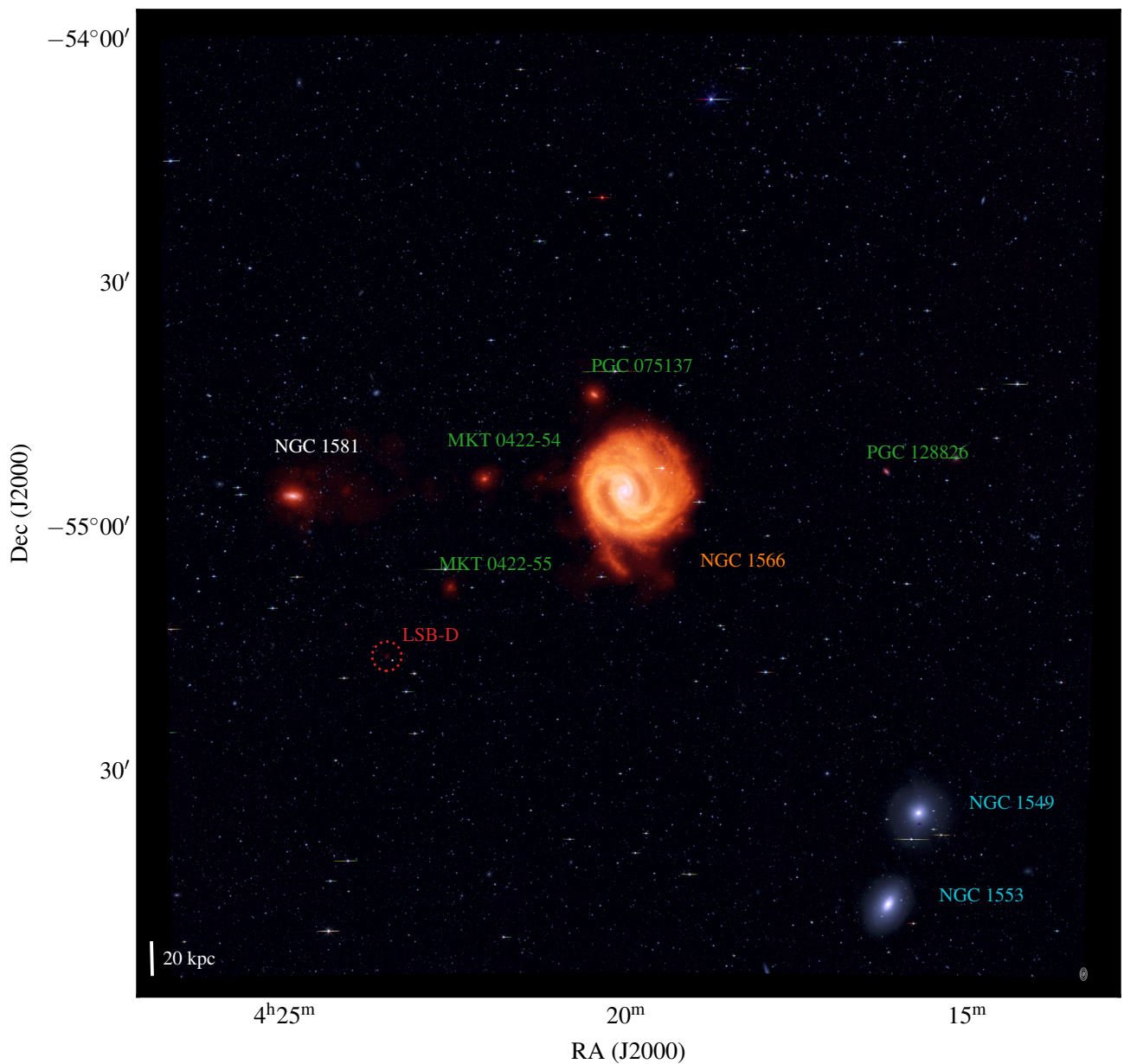


Fig. A.1. Primary beam corrected flux-density HI emission (in orange) detected by MeerKAT, overlaid with the 2×2 degrees DECaLS optical image in the g,r,z filters. The HI emission is an overlay of the flux-density maps extracted from the multi-resolution datacubes (see Sect. 2). The PSFs of the multi-resolution maps varying from $90''$ to $7''$ are shown in white in the bottom-right corner. The target of the MeerKAT observations, NGC 1566, is marked in orange, sources with previously known HI are marked in white, while new HI detections are marked in green. The doublet of early type galaxies in the centre of the Dorado group is marked in cyan. The newly discovered HI low surface brightness galaxy object of this paper is marked by the red circle.

Appendix B: H I clouds in Dorado

Figure B.1, shows the integrated H I profile of a ‘dark’ cloud that may be present at the detection limit of our observations at coordinates: $04^{\text{h}}22^{\text{m}}31^{\text{s}}$, $-55^{\text{d}}12^{\text{m}}02^{\text{s}}$. At $25 \times 18''$, this emission line is unresolved, it is centred at $v_{\text{sys}} = 1292 \text{ km s}^{-1}$ and has full width at zero intensity of $w_{\text{FWZI}} = 18 \text{ km s}^{-1}$. It is best detected after hanning-smoothing the datacube over three channels. The H I integrated flux $S_{1.4\text{GHz}}\Delta v = 5.5 \text{ mJy km s}^{-1}$. At the distance of Dorado, this corresponds to an H I mass of $M_{\text{HI}} = 3.6 \times 10^5 M_{\odot}$. This value is 20% higher than the $S/N = 3$ H I mass detection limit for a source of 16 km s^{-1} in those regions of the primary beam corrected datacube. If real this cloud may be the remnant of the past interaction between NGC 1566 and NGC 1581. The projected distance between this H I cloud and LSB-D is $\sim 8.86'$ ($\sim 45 \text{ kpc}$) and their difference in line of sight velocities is $\Delta v = 78 \text{ km s}^{-1}$. Even though rare, similar ‘dark’ low-column density H I clouds ($N_{\text{HI}} \lesssim 3 \times 10^{19} \text{ cm}^{-2}$) have been detected as remnants of past interactions in groups (see, for example, Serra et al. 2019; Maccagni et al. 2023). Some ‘dark’ clouds also show indications of rotation (e.g. Xu et al. 2023), which could also occur in this newly detected cloud, as suggested by the double peaked profile.

In Fig. B.2 we show the channel maps of the H I emission of LSB-D detected at $25'' \times 18''$ and $32'' \times 23''$ resolution.

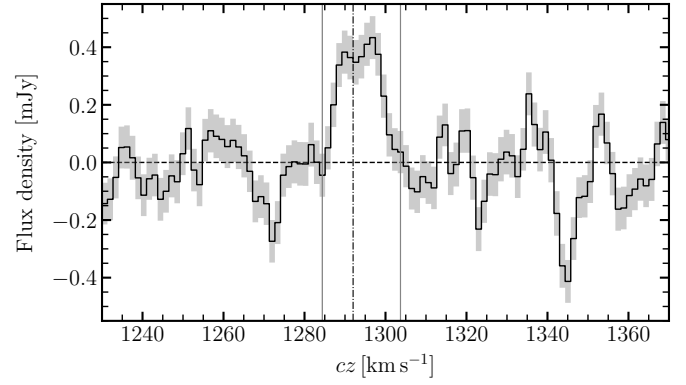


Fig. B.1. Integrated spectrum the ‘dark’ cloud detected at coordinates $04^{\text{h}}22^{\text{m}}31^{\text{s}}$, $-55^{\text{d}}12^{\text{m}}02^{\text{s}}$. The vertical dashed-dotted line shows the central velocity of the H I line ($v_{\text{sys}}^{\text{radio}} = 1292 \text{ km s}^{-1}$), while the grey vertical lines marks its full velocity range ($w_{\text{FWZI}} = 18 \text{ km s}^{-1}$).

The centre of the optical body of the galaxy is marked by the red cross. One every two channel is shown, the H I disk is visible between 1207 km s^{-1} and 1220 km s^{-1} , while the cloud in the north-east is visible at channels 1209 km s^{-1} and 1212 km s^{-1} .

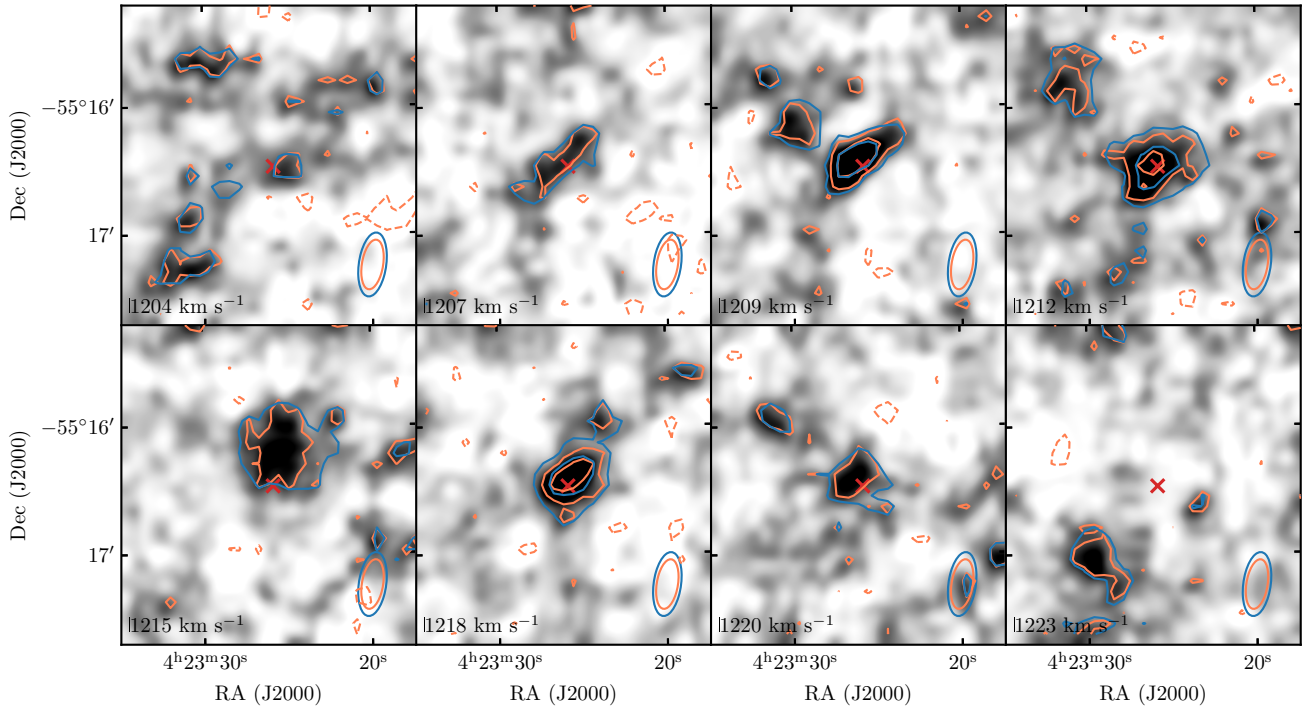


Fig. B.2. Channel maps of the HI emission of LSB-D maps from the r10 and r15 datacubes (orange and blue contours, respectively). One every two channels is shown, contour levels increase as $2.5\sigma \times 2^n$ ($n = 0, 1$). The red cross marks the centre of the optical body of the galaxy. The PSFs of the datacubes are shown in the bottom left corner.

Appendix C: Deprojected coordinates of LSB-D derived from orbit catalogues

In Sect. 3 we provide the probability for LSB-D to be a recent infaller of the Dorado group based on the probability distribution of its orbital parameters and deprojected coordinates of galaxies in groups and clusters of an N-body simulation. Here, we describe more in detail the methodology which follows Oman et al. (2021). The input orbit catalogue is compiled from an N-body simulation of the same $(100 \text{ Mpc})^3$ volume used in the EAGLE (Schaye et al. 2015) project (with a particle mass of $1.2 \times 10^7 M_\odot$) run to a final scale factor of two. Dorado's virial mass and radius (see Table 1) correspond to an overdensity $\Delta_{\text{vir}} = M_{\text{vir}}/(\rho_{\text{crit}} \frac{4}{3} \pi r_{\text{vir}}^3) = 220$. Assuming a Navarro et al. (1997) density profile and a concentration parameter $c_{200} = 10$ we convert to the virial definition used in Oman et al. (2021) and calculate the corresponding 3D velocity dispersion using their Eq. 1. The values used in this context are: $M_{\text{vir}} = 4.1 \times 10^{13} M_\odot$; $r_{\text{vir}} = 873 \text{ kpc}$; $\sigma_{3\text{D}} = 571 \text{ km s}^{-1}$. Assuming NGC 1553 as the group centre gives normalised offsets of $r/r_{\text{vir}} = 0.40$ and $(v_{\text{sys}} - v_{\text{Group}})/\sigma_{3\text{D}} = 0.02$. We select satellites from the orbit catalogue where: (i) the host mass is within 0.2 dex of M_{vir} ; (ii) the normalised radial offset is within ± 0.1 of that of LSB-D; (iii) the absolute value of the normalised LoS velocity offset is less than 0.12 (the absolute value reflects the degeneracy between the sign of the velocity offset and whether LSB-D is in the foreground or background of the group); (iv) the satellite halo peak mass (maximum bound mass at any earlier time) is within 0.5 dex of $10^8 M_\odot$. The last element of the selection, (iv), is the most uncertain, but the HI kinematics and stellar mass of LSB-D suggest a total mass of about $10^8 M_\odot$ – and the probability distributions obtained from the orbit library are only weakly sensitive to this choice.

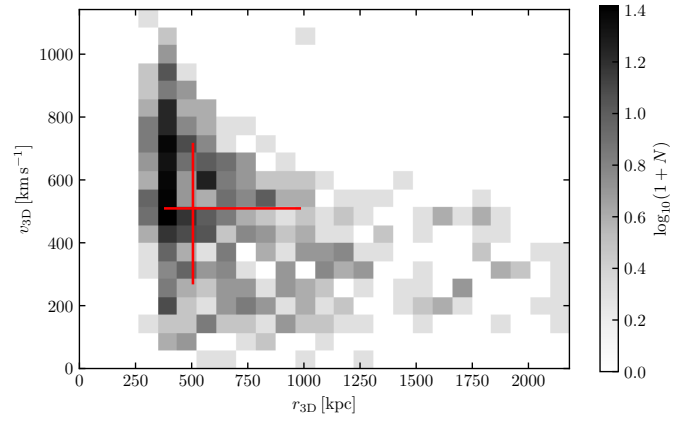


Fig. C.1. Deprojected coordinates of LSB-D derived from orbit catalogues following the methodology of Oman et al. (2021) as detailed in Sec. 3.1. The grayscale map shows a histogram of the deprojected coordinates for simulated satellites with projected coordinates, host mass and satellite mass compatible with those of LSB-D. The red lines mark the median and 16th-84th percentiles of the marginalised probability distributions for the deprojected radius $r_{3\text{D}}$ and current speed $v_{3\text{D}}$.